



## Multiple fluids involved in granite-related W-Sn deposits from the world-class Jiangxi province (China)

Hélène Legros, Antonin Richard, Alexandre Tarantola, Kalin Kouzmanov, Julien Mercadier, Torsten Vennemann, Christian Marignac, Michel Cuney, Ru-Cheng Wang, Nicolas Charles, et al.

### ► To cite this version:

Hélène Legros, Antonin Richard, Alexandre Tarantola, Kalin Kouzmanov, Julien Mercadier, et al.. Multiple fluids involved in granite-related W-Sn deposits from the world-class Jiangxi province (China). *Chemical Geology*, 2019, 508, pp.92-115. 10.1016/j.chemgeo.2018.11.021 . hal-02334110

**HAL Id: hal-02334110**

**<https://hal.science/hal-02334110>**

Submitted on 22 Oct 2021

**HAL** is a multi-disciplinary open access archive for the deposit and dissemination of scientific research documents, whether they are published or not. The documents may come from teaching and research institutions in France or abroad, or from public or private research centers.

L'archive ouverte pluridisciplinaire **HAL**, est destinée au dépôt et à la diffusion de documents scientifiques de niveau recherche, publiés ou non, émanant des établissements d'enseignement et de recherche français ou étrangers, des laboratoires publics ou privés.



Distributed under a Creative Commons Attribution - NonCommercial 4.0 International License

**Revision 2**

**Multiple fluids involved in granite-related W-Sn deposits from the world-class Jiangxi province (China)**

Hélène Legros <sup>a,b,\*</sup>, Antonin Richard <sup>a</sup>, Alexandre Tarantola <sup>a</sup>, Kalin Kouzmanov <sup>c</sup>, Julien Mercadier <sup>a</sup>, Torsten Vennemann <sup>d</sup>, Christian Marignac <sup>a,e</sup>, Michel Cuney <sup>a</sup>, Ru-Cheng Wang <sup>f</sup>, Nicolas Charles <sup>b</sup>, Laurent Bailly <sup>b</sup>, Marc-Yves Lespinasse <sup>a</sup>

<sup>a</sup> *Université de Lorraine, CNRS, GeoRessources, Boulevard des Aiguillettes B.P. 70239, F-54506 - Vandoeuvre-lès-Nancy, France*

<sup>b</sup> *BRGM-French Geological Survey, 3, Av. Claude Guillemin, BP 36009, 45060 Orléans Cedex 2, France*

<sup>c</sup> *Département des Sciences de la Terre, Université de Genève, Rue des Maraîchers 13, 1205 Genève, Switzerland*

<sup>d</sup> *Institut des Sciences de la Terre, Université de Lausanne, Quartier UNIL-Mouline, Bâtiment Géopolis, CH-1015 Lausanne, Switzerland*

<sup>e</sup> *Ecole Nationale Supérieure des Mines de Nancy, Parc de Saurupt, F-54042 Nancy, France*

<sup>f</sup> *State Key Laboratory for Mineral Deposits Research, School of Earth Sciences and Engineering, Nanjing University, Xianlin University Town, Nanjing 210046- China*

\* Present address: Department of Earth and Atmospheric Sciences, University of Alberta, 1-26 Earth Sciences Building, Edmonton, Alberta, Canada T6G 2E3

Email: [hlegros@ualberta.ca](mailto:hlegros@ualberta.ca)

## 24   **Abstract**

25

26   This paper aims at providing new insights into W-Sn ore-forming processes within one of the  
27   largest granitic provinces in the world (Nanling Range, South China), which was emplaced  
28   during the Jurassic-Cretaceous period. The origin, composition and pressure-temperature  
29   conditions of fluids involved in the W-Sn ore-forming processes have been investigated by  
30   microthermometry, Raman spectroscopy, LA-ICPMS, hydrogen isotope analyses of fluid  
31   inclusions and oxygen isotope analyses of minerals from the Maoping and Piaotang W-Sn  
32   deposits. For each deposit, pre- (quartz), syn- (wolframite and cassiterite) and post-ore  
33   (quartz, topaz and fluorite) minerals were studied.

34   In both deposits, the vast majority of fluid inclusions are aqueous with salinities between 0.0  
35   and 12.6 wt. % equiv. NaCl and homogenization temperatures between 136 and 349 °C. A  
36   minor proportion (~5%) of inclusions observed in the ore-stage quartz from Maoping have  
37   aquo-carbonic compositions. For both deposits, four compositional groups are defined. Early  
38   quartz fluid inclusions are characterized by salinities between 0.4 and 9.0 wt. % equiv. NaCl,  
39   trapping temperatures between 150 and 350 °C, and pressures between 20 and 150 MPa. LA-  
40   ICPMS analyses of these fluid inclusions reveal a wide range of Na, K and Li concentrations,  
41   as well as relatively low metal contents ( $W < 40$  ppm). Values of  $\delta^{18}\text{O}$  in quartz range from -  
42   3.6 to 5.3 ‰ VSMOW while  $\delta\text{D}$  values of the fluid inclusions range from -59 to -51 ‰  
43   VSMOW. The salinity of fluid inclusions in wolframite, cassiterite, topaz and fluorite is  
44   between 2.4 and 11.2 wt. % equiv. NaCl, trapping temperatures are between 200 and 600 °C,  
45   and pressures range from 20 to 250 MPa. LA-ICPMS analyses of these fluid inclusions reveal  
46   higher concentrations of Na, K and Li as well as Cs and metals (*e.g.* between 10 and 220 ppm  
47   W). Values of  $\delta^{18}\text{O}$  in wolframite, cassiterite, topaz and fluorite crystals range from -3.0 to 3.3

48 ‰ VSMOW while  $\delta D$  values of fluid inclusions in these mineral phases range from -78 to -72  
49 ‰ VSMOW.

50 At Piaotang, fluid inclusions in wolframite as well as in post-ore quartz and fluorite have  
51 salinities of 5.6 to 12.6 wt.% eq. NaCl, trapping temperatures between 150 and 400 °C and  
52 pressures of 20 to 150 MPa. LA-ICPMS analyses of these fluid inclusions reveal similar  
53 compositions to early quartz fluid inclusions. Values of  $\delta^{18}O$  in wolframite and quartz crystals  
54 range from -0.8 to 5.2 ‰ VSMOW, while the  $\delta D$  values of fluid inclusions range from -66 to  
55 -62 ‰ VSMOW.

56 Collectively, the data suggest the involvement of four aqueous fluid end-members, mixed  
57 episodically in the mineralization process: (A) a low-salinity, low-temperature, metal-poor,  
58 low- $\delta^{18}O$ , low- $\delta D$  fluid derived from meteoric water; (B) a high-salinity, high-temperature,  
59 metal-poor, high- $\delta^{18}O$ , low- $\delta D$  fluid derived from a differentiated peraluminous granitic  
60 magma; (C) a high-salinity, high-temperature, metal-rich, lower  $\delta D$  magmatic fluid derived  
61 from a more differentiated peraluminous granitic magma; and (D) a high-salinity, high-  
62 temperature, metal-rich, high- $\delta^{18}O$ , low- $\delta D$  magmatic fluid.

63 This study shows that multiple fluids with distinct magmatic and meteoric origins were  
64 involved in the formation of these W-Sn deposits and that the dilution of metal-bearing  
65 magmatic fluids by meteoric fluids was probably the main driver for ore deposition. The  
66 common fluid history of the two deposits studied, as well as similarities with other deposits in  
67 the Jiangxi province, points towards common ore-forming processes at the regional scale.

68

## 69 **Keywords**

70

71 W-Sn deposits, fluid inclusions, Maoping, Piaotang, China

72



## 73 1. Introduction

74

75 In granite-related W-Sn deposits, the world's main W and Sn resource, magmatic and  
76 hydrothermal activity are thought to have promoted the formation of ore minerals in and  
77 around peraluminous granitic plutons (Burnham, 1979; Candela, 1997; Audétat *et al.*, 2000;  
78 Mao *et al.*, 2007; Xi *et al.*, 2007; Pirajno, 2009; Zhou *et al.*, 2010). However, the nature and  
79 the origin of the ore-forming fluids appear to be variable and are still debated (*e.g.*, Marignac  
80 and Cathelineau, 2009). Most models involve (i) high-salinity magmatic-hydrothermal fluids  
81 exsolved from the granitic magmas (Audétat *et al.*, 2000; Kamenetsky *et al.*, 2004; Thomas *et al.*,  
82 2005; Korges *et al.*, 2017; Lecumberri-Sanchez *et al.*, 2017), and/or (ii) “external”  
83 hydrothermal fluids of deep-seated or surficial origin, characterized by variable volatile and  
84 salt contents and equilibrated to variable degrees with the granites and their metamorphic  
85 hosts (Weisbrod 1988; Wilkinson 1990; Blamart 1991; Noronha *et al.*, 1992; Smith *et al.*,  
86 1996; Bebout *et al.*, 1999; Polya *et al.*, 2000; Burnard and Polya 2004; Cai *et al.*, 2007).

87 In the present study, two W-Sn deposits (Maoping and Piaotang) were targeted as  
88 representative of the Jiangxi province, which forms part of the world's richest W and Sn  
89 province, the Nanling Range in China (USGS, 2017). The Nanling Range is a metallogenic  
90 province in which multiple and diverse mineral deposits (W, Sn, Cu, Pb-Zn, etc.) are  
91 associated with one of the largest granitic provinces in the world (100,000 km<sup>2</sup>), emplaced  
92 during Jurassic-Cretaceous times (Zaw *et al.*, 2007).

93 Several fluid inclusion (FI) studies have already been carried out in W-Sn deposits from the  
94 Nanling Range, involving microthermometry (in transparent and opaque minerals), Raman  
95 spectroscopy, stable isotope (O, H, S, C) analyses and noble gas isotope (He, Ar) analyses  
96 (Giuliani *et al.*, 1988; Xuexin *et al.*, 1990; Zeng *et al.*, 2002; Xi *et al.*, 2008; Cao *et al.*, 2009;  
97 Wang *et al.*, 2009; Feng *et al.*, 2012; Gong *et al.*, 2015; Hu *et al.*, 2012; Wang *et al.*, 2012;

Wei *et al.*, 2012; Zhang *et al.*, 2012; Ni *et al.*, 2015; Xiong *et al.*, 2017; Chen *et al.*, 2018). All of these studies point to mixing between a magmatic fluid exsolved from a peraluminous granitic magma and a meteoric fluid as being responsible for ore mineral precipitation. However, detailed petrographic and mineralogical studies coupled with Fe-Li-mica geochemistry in the Maoping and Piaotang deposits suggest that three to four types of fluid, mixed to variable degrees, were involved (Legros *et al.* 2016 and 2018). Motivated by the possibility that multiple types of fluid were involved, in contrast with the single-fluid or two-fluid models mentioned above, we decided to undertake the first-ever detailed characterization of the fluids by microthermometry (pressure-temperature-composition properties of FIs), Raman spectroscopy (volatile content of the FIs), stable isotope analysis (H and O isotopic compositions of FIs and host minerals, respectively), and LA-ICPMS (major and trace element compositions of FIs). Economic minerals (wolframite, cassiterite) and gangue minerals (quartz, topaz, and fluorite) were studied in order to investigate, for the first time, the evolution of the fluids from the pre-ore to the post-ore stage using multiple analytical methods.

## **2. Geological setting and previous fluid inclusion studies**

### **2.1 The southern Jiangxi metallogenic province (Nanling Range)**

The southern Jiangxi province contains 90% of China's tungsten resources (Zeng *et al.* 2007), including 429 deposits with total reserves of 1.7 Mt WO<sub>3</sub>. The province is located within the Nanling Range, in the Cathaysia Block of the South China Craton (SCC). The SCC formed during the late Proterozoic Jiangnan (or Sibao) orogeny by the suturing of the Yangtze Block to the north and the Cathaysia Block to the south (Fig. 1; Charvet 2013 and

references therein). The Sibao orogeny, dated to between 1040 and 900 Ma by U-Pb (zircon) and  $^{40}\text{Ar}/^{39}\text{Ar}$  (muscovite) methods, formed as a result of diachronous closure of the ocean between the Cathaysia and Yangtze Blocks during the assembly of Rodinia (Li *et al.* 2007). The boundary between these two blocks, bordering the orogenic belt to the south-east, is generally considered to be marked by the Jiangshan-Shaoxi fault zone, which marked by a drop in the depth of the Moho of several Kilometers in this zone (Wang *et al.*, 2013 and references therein).

From the late Neoproterozoic onwards, the South China Craton was strongly reworked and progressively meta-cratonized by multiple intracontinental episodes, starting with the major aborted Nanhua rifting episode (Wang *et al.*, 2006). The latter was followed by the bivergent NE-trending Kwangsi orogeny (Ordovician-Devonian), which resulted from inversion of the Nanhua rift (Charvet *et al.*, 2010 and 2013), and multiple metamorphic events that peaked at 720 °C and 1030 kbar at around 450 Ma.

The Indosinian (Permian-Triassic) orogeny then overprinted the Proterozoic deformations of the Jiangnan belt in the Cathaysia. This orogeny was marked by extensive granitic magmatism that spanned more than 60 Myr (265-205 Ma; Mao *et al.*, 2012 and references therein) and covered a 14,300 km<sup>2</sup> area (Sun *et al.*, 2012).

Finally, the Yanshanian orogeny (Jurassic-Cretaceous) generated the most extensive and intense magmatic activity (mainly granitic and rhyolitic) in the region (Li *et al.*, 2014). Three major metallogenic periods are associated with the Yanshanian orogeny: magmatic-related Cu, Pb-Zn and polymetallic mineralization (Jiangxi and southeastern Hunan) between 180 and 170 Ma; rare-metal mineralization (W-Sn, Nb, Ta) related to S-type granitoids from 160 to 139 Ma; and magmatism-related Sn, U, and Au-Cu-Pb-Zn-Ag mineralizations in the Nanling Range and southeast coastal zone (Hua *et al.*, 2005), between 125 and 98 Ma. The W-Sn deposits occur almost exclusively within the outer contact zones of S-type Jurassic

granites, as is the case for the Maoping and Piaotang W-Sn deposits as well as other numerous large W-Sn deposits in the Dayu district of the southern Jiangxi province, dated between 160 and 150 Ma, such as the Xihuashan deposit (Giuliani *et al.*, 1988; Guo *et al.*, 2012; Fig. 1).

## 2.2. Geology of the Maoping and Piaotang deposits

### 2.2.1 Maoping deposit

The Maoping deposit is associated with a buried peraluminous granite (*ca.* 300 m deep) whose contact with the surrounding Cambrian quartzite and schists can only be observed in drill cores. Two types of mineralization associated with this granite have been described: wolframite-cassiterite-quartz veins and disseminated wolframite in the greisen body. A drillcore-based cross-section of the Maoping deposit is presented in Figures 2A and B and shows the greisen orebody at the top of the granitic intrusion and a network of radial, sub-vertical ore-bearing veins, rooted to the top of the granite and mostly developed in the Cambrian host rocks (Feng *et al.*, 2011). More than 400 W-Sn-bearing quartz-dominated veins, 5 cm to a few meters in thickness and up to 400 m in length, have been identified (Feng *et al.*, 2011). It is worth noting that even though only one level in the mine galleries (level -5, *ca.* 200 m depth) was investigated in the present study, all of the veins appeared to be shallow-dipping in the mine gallery, contrary to the cross-section proposed by Feng *et al.* (2011). The granite was emplaced during the Jurassic at  $151.8 \pm 2.9$  Ma (SHRIMP U-Pb zircon dating; Feng *et al.*, 2011), and the greisen and the veins have been dated to  $155.3 \pm 2.8$  and  $150.2 \pm 2.8$  Ma, respectively (Re-Os on molybdenite; Feng *et al.*, 2011). The Maoping deposit is estimated to contain 63 kt WO<sub>3</sub> and 15 kt Sn, with average grades of 0.93 % and 0.3

%, respectively (Feng *et al.*, 2011), and is considered one of the largest W-Sn deposits in the Nanling Range.

A detailed petrographic study of the Maoping deposit was carried out by Legros *et al.* (2016) and the paragenetic succession that was established is summarized here. Four types of vein and seven successive paragenetic stages (I to VII) were identified from petrographic observations and cross-cutting relationships in the mine galleries (Fig. 3). Hereafter, the mineral nomenclature used here refers to (i) the recommended IMA mineral abbreviations, (ii) the generation number (1 to 4, from the oldest to the youngest), and (iii) the stage to which the mineral belongs (I to VII from the earliest to the latest). For example, in Figure 3, Wf<sub>1-III</sub> refers to the first time wolframite crystallized in the system, which was during stage III (the W-Sn stage).

The first stage in the paragenetic sequence, Stage (I), is marked by cm-sized microcline and smaller quartz and Fe-Li-micas that form the earliest veins. These veins were interpreted to be magmatic in origin by Legros *et al.* (2016). The small size of the quartz crystals meant that FI analysis was not possible for this vein type. The second stage (II) is characterized by hydrothermal veins filled with Fe-Li-mica only. Stages III to VI correspond to W-Sn and banded-quartz veins and involved the successive crystallization of various minerals that are suitable for FI study, as described in more detail below.

Stage III corresponds to the formation of the ore-bearing veins (Fig. 4A). During Stage III, quartz (Qtz<sub>2,3-III</sub>), topaz (Toz<sub>2-III</sub>), wolframite (Wf<sub>1-III</sub>), cassiterite (Cst<sub>1-III</sub>), Fe-Li-micas (Fe-Li-mca<sub>3-III</sub>), molybdenite (Mlb<sub>1-III</sub>), Li-Fe muscovite (Li-Fe-ms<sub>1-III</sub>) and Fe-Mn hydroxides were successively deposited. Quartz and topaz are abundant in the veins and form geodic crystals with no apparent zoning (Fig. 4B). Wolframite and cassiterite crystallized next, as euhedral and well-zoned crystals (Fig. 4C and 4D). Evidence for ductile deformation during this stage allows two successive episodes (syn-deformation IIIa and post-deformation IIIb) to be

distinguished. The deformation is particularly well-developed in quartz and topaz minerals, where undulose extinction and elongated subgrains are observed. Wolframite and cassiterite also show marked evidence for plastic deformation, with folded crystals but no signs of recrystallization. Stage IIIb is characterised by the presence of undeformed Li-Fe-ms<sub>I-III</sub> and Fe-Mn hydroxides.

Stage IV corresponds to the emplacement of banded quartz veins (Fig. 4E). Four types of undeformed quartz can be distinguished. The banding was formed by a repeated sequence of (1) quartz corrosion, (2) the accumulation of minerals (feldspars, micas and quartz), interpreted to be relics of minerals from previous stages, together with precipitation of disseminated Nb-Ta and REE minerals and Qtz<sub>4a-IV</sub>, (3) deposition of Qtz<sub>4b-IV</sub>, and (4) deposition of laminated Qtz<sub>4c-IV</sub>. A final generation of subhedral Qtz<sub>4d-IV</sub> overprints the quartz banding (Fig. 4F). Given the similar results obtained for FIs in Qtz<sub>4a-IV</sub>, Qtz<sub>4b-IV</sub>, Qtz<sub>4c-IV</sub> and Qtz<sub>4d-IV</sub>, these four types are grouped together as Qtz<sub>4-IV</sub> and will no longer be distinguished.

Stage V is marked by rare and very small quartz grains (< 0.1 mm), Li-muscovite, and sulphides and does not contain any mineral of interest for this FI study.

Stage VI consists of a succession of fluorite (Fl<sub>1-VI</sub>), kaolinite (Kln<sub>1-VI</sub>) and late porous fluorite (Fl<sub>2-VI</sub>) that fills the cavities of the W-Sn and banded quartz veins (Fig. 4G). Dissolution cavities in Toz<sub>2-III</sub> are filled by Kln<sub>1-VI</sub> and have rims composed of euhedral and zoned Toz<sub>4-VI</sub> crystals (more than 100 µm in size) (Fig. 4H). The last generation of topaz was selected for the FI study. The first generation of fluorite (Fl<sub>1-VI</sub>) is euhedral, mineral inclusion-free and is coeval with the kaolinite. The second generation (Fl<sub>2-VI</sub>) postdates the kaolinite and is anhedral and zoned. The zoning is associated with variation in the yttrium content, kaolinite inclusions, REE mineral inclusions (phosphates, fluorides and carbonates) and porosity. Both generations of fluorite were selected for the FI study.

Stage VII displays sulphides (*e.g.* bismuthinite and pyrite) that were not considered for the FI study.

### 2.2.2 Piaotang deposit

The Piaotang deposit is associated with a hidden biotite granite intrusion (*ca.* 400 m deep), the contact of which with the surrounding metasedimentary rocks can only be observed in drill cores. Two types of mineralization are described: wolframite-cassiterite-quartz veins and disseminated wolframite in the greisen. The polymetallic W-Sn-(Nb) Piaotang deposit, located near the Xihuashan deposit, is one of the largest W-Sn deposits in the Nanling Range (Fig. 2C). The Piaotang mine produces 1.5 kt WO<sub>3</sub> per year and ranks eighth largest of China's reserves with 47 kt WO<sub>3</sub> (MB Company database: [www.metalbulletin.com](http://www.metalbulletin.com)). A drillcore-based cross-section of the Piaotang deposit has been established and shows steeply-dipping sub-parallel veins rooted in the buried granitic intrusion and hosted in the metasedimentary rocks (Ni *et al.*, 2015). The greisen cupola was not captured in the original cross-section of Ni *et al.* (2015), and it was not possible to precisely document the extent of the greisen and its relationship with the granite in the present study (Fig. 2D). The granite was emplaced during the Jurassic ( $159.8 \pm 0.3$  Ma, U-Pb dating on zircon; Zhang *et al.*, 2017). The greisen has not yet been dated but an age of  $159.5 \pm 1.5$  Ma has been determined for the veins (U-Pb dating on cassiterite; Zhang *et al.*, 2017).

One type of vein with heterogeneous ore infilling was identified in the mine galleries of the Piaotang deposit by Legros *et al.* (2018). The thickness of this vein type decreases from the top to the bottom of the vein system, from a few centimetres at 556m depth to more than one meter at 268m depth. Based on petrographic observations, Legros *et al.* (2018) distinguished four paragenetic stages (I to IV) at the Piaotang deposit (Fig. 5).

Stage I corresponds to the precipitation of the ore-minerals (Fig. 6A and 6B): wolframite (Wf<sub>I-1</sub>), quartz (Qtz<sub>I-1</sub>), cassiterite (Cst<sub>I-1</sub>), Fe-Li-micas (Fe-Li-mca<sub>I-1 to 3-1</sub>), topaz (Toz<sub>I-1</sub>) and molybdenite (Mlb<sub>I-1</sub>). Quartz is the most abundant mineral in the vein and is present as cm-sized euhedral crystals that do not exhibit the chemical zoning observed in cassiterite (Fig. 6C and 6D). All three minerals were selected for the FI study. Topaz is almost completely altered into clay minerals and no FIs were observed.

Plastic deformation occurred during Stage I. As described in Legros *et al.* (2018), this deformation is particularly evident within quartz, topaz and micas, which show low intensity kinking and the formation of sub-grains, and to a lesser extent in wolframite, which presents slightly folded crystals (Fig. 6C).

Stage II corresponds to the replacement of Wf<sub>I-1</sub> by scheelite (Sch<sub>I-II</sub>) and the crystallization of chlorite (Chl<sub>I-II</sub>), columbo-tantalite (Clb<sub>I-II</sub>) and fluorite (Fl<sub>I-II</sub>). The fluorite forms euhedral cm-sized crystals that exhibit no zonation, mineral inclusions or plastic deformation (Fig. 6B), and was selected for the FI study.

Stages III and IV were characterized by significant sulphide precipitation together with new generations of wolframite, cassiterite, Fe-Li-micas, chlorite and fluorite. Minerals from Stages III and IV are all too small for FI analysis.

### 2.3. Previous fluid inclusion studies of W-Sn deposits in the Nanling Range

Several vein-type granite-related W-Sn deposits in the Nanling Range, and more precisely within the southern Jiangxi and Hunan provinces, have been the subject of FI studies: Xihuashan (Giuliani *et al.*, 1988; Wei *et al.*, 2012), Maoping (Chen *et al.*, 2018), Yaogangxian (Hu *et al.*, 2012), Dajishan, Dangping, Piaotang, Pangushan (Ni *et al.*, 2015), Taoxikeng (Wang *et al.*, 2012), Shimenshi (Gong *et al.*, 2015; Wei *et al.*, 2017), Baxiannao



271 (Feng *et al.*, 2012), Shizhuyuan and Yejiwei (Xuexin *et al.*, 1990). Fluid inclusion studies  
 272 have been carried out on various transparent and opaque minerals from the vein systems,  
 273 including beryl, quartz, wolframite, cassiterite, fluorite, and tourmaline. Fluids are dominantly  
 274 aqueous, but CO<sub>2</sub>-rich FIs are sometimes observed in quartz and very rarely in wolframite.  
 275 Vapor-dominated CO<sub>2</sub>-rich FIs that coexist with liquid-dominated aqueous FIs are commonly  
 276 observed in quartz and have been interpreted as being related to boiling and/or immiscibility  
 277 (Wei *et al.*, 2012; Giuliani *et al.*, 1988; Ni *et al.*, 2015). Nevertheless, most inclusions  
 278 observed in wolframite and cassiterite are aqueous and can be used to unravel differences in  
 279 the fluid conditions of ore and gangue minerals (Piaotang, Dangping, Dajishan, Pangushan,  
 280 Ni *et al.*, 2015; Xihuashan, Wei *et al.*, 2012). Microthermometry data indicate  
 281 homogenization temperatures ( $T_h$ ) of 150 to 300 °C for the gangue minerals, significantly  
 282 lower than those of wolframite (250 and 400 °C). Similarly, FIs in gangue minerals have a  
 283 lower salinity (0.5 to 9.0 wt.% equiv. NaCl) than those in wolframite (3.0 to 14.0 wt.% equiv.  
 284 NaCl) (Xihuashan, Giuliani *et al.*, 1988; Maoping, Chen *et al.*, 2018; Shizhuyuan, Yejiwie,  
 285 Xuexin *et al.*, 1990; Piaotang, Zeng *et al.*, 2002, Wang *et al.*, 2009; Dajishan, Xi *et al.*, 2008;  
 286 Yaogangxian, Cao *et al.*, 2009; Baxiannao, Feng *et al.*, 2012; Taoxikeng, Wang *et al.*, 2012;  
 287 Dangping, Pangushan, Ni *et al.*, 2015; Shimenshi, Wei *et al.*, 2017). Within single deposits,  
 288 wolframite FIs usually display a continuum between a high-salinity, high-temperature end-  
 289 member and a low-salinity, low-temperature end-member, interpreted as a mixing trend. A  
 290 combination of mixing and cooling processes has been considered decisive for ore mineral  
 291 precipitation (Wei *et al.*, 2012; Ni *et al.*, 2015; Chen *et al.*, 2018). Estimated P-T conditions of  
 292 FI entrapment in the Xihuashan, Dajishan and Taoxikeng deposits, assuming hydrostatic  
 293 pressure conditions and a geothermal gradient of around 50°C/km, range from 40 to 130 MPa  
 294 and 320 to 400 °C (Wei *et al.*, 2012; Xi *et al.*, 2008; Wang *et al.*, 2012). Pressure estimates  
 295 define depths of emplacement of between 1 and 4 km (Xuexin *et al.*, 1990; Wang *et al.*,

2012). Stable isotope analyses (O-H-S) have been performed on quartz, wolframite and sulphide minerals, and also on quartz-hosted FIs from the Xihuashan, Taoxikeng, Shimenshi and Baxiannao deposits and on a few wolframite-hosted FIs from the Maoping deposit. In all deposits,  $\delta^{18}\text{O}$  values of quartz and wolframite range from -8.8 to 14.3 ‰ and 4.1 to 6.0 ‰ VSMOW, respectively,  $\delta\text{D}$  values of quartz- and wolframite-hosted FIs range from -83 to 108 ‰ and -64 to -49 ‰, respectively, and  $\delta^{34}\text{S}$  values of late sulfides range from -1.6 to 0.1 ‰ (Feng *et al.*, 2012; Liu *et al.*, 2002; Wang *et al.*, 2012; Wei *et al.*, 2012; Gong *et al.*, 2015; Wei *et al.*, 2017). Helium and argon isotope compositions of wolframite- and sulfide-hosted inclusions from the Piaotang and Yaogangxian deposits ( $^3\text{He}/^4\text{He} = 0.2\text{--}0.8 \text{ R/R}_A$  and  $^{40}\text{Ar}/^{36}\text{Ar} = 350\text{--}590$ ; Wang *et al.*, 2009; Hu *et al.*, 2012).

In summary, taken together, the previous FI studies of vein-type granite-related W-Sn deposits in the Nanling Range point to compositions and conditions that can be interpreted as reflecting either mixing of two fluids (magmatic dominant and meteoric minor) or cooling of a single fluid (magmatic), either of which could have led to the precipitation of the ore minerals.

### 3. Samples and analytical methods

#### 3.1 Fluid inclusion petrography and microthermometry

Double-polished thick sections (110 to 200  $\mu\text{m}$  thick) of quartz, cassiterite, wolframite, fluorite and topaz samples were prepared at the GeoRessources laboratory (Nancy, France). Sections were made from multiple samples from each deposit (Maoping deposit (Stages III, IV and VI): Qtz<sub>2-III</sub> = 3 samples, Wf<sub>1-III</sub> = 6 samples, Cst<sub>1-III</sub> = 3 samples, Qtz<sub>4-IV</sub> = 4 samples, Fl<sub>1-VI</sub> = 3 samples, Toz<sub>4-VI</sub> = 3 samples, Fl<sub>2-VI</sub> = 1 sample. Piaotang deposit (Stages I and II):

321 Qtz<sub>I-I</sub> = 4 samples, Wf<sub>I-I</sub> = 1 sample, Cst<sub>I-I</sub> = 3 samples, and Fl<sub>I-II</sub> = 3 samples). Petrographic  
 322 examinations were performed on transparent and semi-opaque minerals (quartz, cassiterite,  
 323 fluorite and topaz) using an Olympus BX-51 optical microscope at GeoRessources laboratory  
 324 (Nancy, France) and on opaque minerals (wolframite) using an Olympus BH-51 microscope,  
 325 equipped with an Olympus XM-10 infrared camera at the University of Geneva (Switzerland).  
 326 Petrographic observations were made at the scale of the entire crystal in order to compare FIs  
 327 in different growth zones and/or subgrains of the crystals. Cathodoluminescence (CL)  
 328 imaging was also conducted, using a CITL cold cathode instrument CL8200 Mk4 (15 kV and  
 329 400 mA) at the Georessources laboratory (Nancy, France).  
 330 Microthermometry was performed on quartz-, fluorite- and topaz-hosted FIs using a Linkam  
 331 THMSG600 heating-cooling stage mounted on an Olympus BX-51 microscope at the  
 332 GeoRessources laboratory (Nancy, France). The stage was calibrated with in-house and  
 333 certified standards by measuring the temperatures of the final melting of pure water in a silica  
 334 glass capillary (0.0 °C), the triple point of CO<sub>2</sub> ± Ar in a synthetic FI (−56.9 °C), and the  
 335 liquid + vapor → liquid homogenization of a natural FI at 165 °C. In aqueous FIs, the  
 336 temperatures of two phase changes were recorded: final ice melting ( $T_m(\text{ice})$ ) and liquid +  
 337 vapor → liquid total homogenization ( $T_h$ ). For aquo-carbonic FIs, temperatures of final  
 338 clathrate melting ( $T_m(\text{cla})$ ) and liquid + vapor → vapor homogenization of the CO<sub>2</sub>-dominated  
 339 carbonic phase ( $T_h(\text{CO}_2)$ ) were also measured. The temperatures of the phase transitions are  
 340 reported with an accuracy of about ±0.1 °C for  $T_m(\text{ice})$ ,  $T_m(\text{cla})$  and  $T_h(\text{CO}_2)$ , and ±1 °C for  $T_h$ .  
 341 Microthermometry of wolframite-hosted FIs was carried out at the University of Geneva  
 342 (Switzerland) using a Linkam FTIR 600 stage mounted on an Olympus BH-51 microscope  
 343 equipped with an Olympus XM-10 infrared camera (Ortelli *et al.*, accepted). An oriented  
 344 section of a single prismatic crystal cut perpendicular to the cleavage was used. It has been  
 345 demonstrated that the visible light absorbed by opaque minerals is partially converted into

346 heat in proportion to the opacity, and this could potentially preclude accurate  
347 microthermometric measurements (Moritz, 2006). To avoid this problem, a voltmeter was  
348 connected directly to the lamp of the microscope to control the power of the incident light.  
349 Sample heating is not high enough to affect microthermometric measurements if a 90% closed  
350 diaphragm, a condenser at 0.3, and a power of 0 to 4 V depending on the transparency of the  
351 different zones of the crystals are used (Casanova *et al.*, accepted).  
352 Since cassiterite is a semi-opaque mineral, the same protocol as that used for opaque minerals  
353 was applied under transparent light at the GeoRessources laboratory (Nancy, France). Sample  
354 heating due to visible light absorption was negligible compared to wolframite. Analyses were  
355 performed with a fully open diaphragm and condenser, and within a range of 0 to 6 V  
356 depending on the transparency of the different zones in the crystals.  
357 The salinities of CO<sub>2</sub>-rich FIs were calculated using the equation of state of Duan *et al.*,  
358 (1992) in the Q2 programs of Bakker (1997, 2003). The first ice melting temperature (*e.g.* the  
359 eutectic temperature) could not be precisely observed, but the range of the likely transition (-  
360 25 to -15 °C) encompasses the eutectic temperatures of the H<sub>2</sub>O-NaCl and H<sub>2</sub>O-KCl-NaCl  
361 systems (-21.2 °C and -23.5 °C, respectively). In addition to sodium, potassium was identified  
362 by LA-ICPMS in almost all FIs. However, FI compositions cannot be reconstructed in the  
363 H<sub>2</sub>O-NaCl-KCl system in the absence of halite and sylvite at room temperature (Bodnar  
364 2003). Nevertheless, the maximum error in the calculated salinity induced by assuming a  
365 single-salt H<sub>2</sub>O-NaCl system would be *ca.* 1 wt.% equiv. NaCl. Similarly, calcium was  
366 detected by LA-ICPMS in significant amounts in some FIs, sometimes at an even higher  
367 concentration than Na and K. Due to the high limits of detection for calcium in LA-ICPMS  
368 analyses, we cannot exclude the possibility that all of the analyzed FIs contain significant  
369 amounts of calcium. However, no hydrohalite was observed during the microthermometry  
370 runs and the composition of the fluid inclusions cannot therefore be interpreted in the H<sub>2</sub>O-

NaCl-CaCl<sub>2</sub> system. The salinity of aqueous FIs were therefore calculated in the H<sub>2</sub>O-NaCl system using the Archer (1992) equation of state and the Bulk program of Bakker (1997, 2003). Isochores were calculated for aqueous FIs using the ISOC program (Bakker, 1993) and the empirical equations of state of Bodnar and Vityk (1994). All isochores were constructed to reflect hydrostatic conditions and a depth of emplacement of between 5 and 10 km. Evidence for plastic deformation during the main ore event is observed in both deposits and could be indicative of lithostatic conditions. However, the pressure variation that would be associated with the change from lithostatic to hydrostatic conditions does not seem realistic. Moreover, most vein systems are interpreted in terms of hydrostatic conditions.

### 3.2 Raman spectroscopy

Raman spectroscopy of the liquid phase of one-phase liquid aqueous inclusions and of the gas phases of two-phase aqueous incusions and three-phase (liquid H<sub>2</sub>O + liquid CO<sub>2</sub> + vapor CO<sub>2</sub>) inclusions was performed at the GeoRessources laboratory (Nancy, France) in order to detect possible gases and determine their nature. Raman spectra were recorded using a LabRAM HR spectrometer (Horiba Jobin Yvon) equipped with a 600 gr.mm<sup>-1</sup> grating and an edge filter. The confocal hole aperture was 500 µm and the slit aperture was 100 µm. The excitation beam was provided by a Stabilite 2017 Ar<sup>+</sup> laser (Spectra Physics, Newport Corporation) at 514.53 nm and a power of 200 mW, focused on the sample using a 100x objective (Olympus). The acquisition time and number of accumulations were chosen in such a way as to optimize the signal-to-noise ratio (S/N) (ideally lower than 1 %). Neither limits of detection nor absolute concentrations of trace gases could be determined with precision, however the relative proportions of the gas species could be estimated qualitatively using the

peak area, acquisition time, and the specific scattering cross-section of each peak with LabSpec software (Schrotter and Klockner, 1979) as defined by Burke (2001).

### 3.3 LA-ICPMS analysis

Selected major, minor and trace elements were measured in FIs in quartz, cassiterite, topaz and fluorite using the LA-ICPMS instrumental setup at the GeoRessources laboratory (Nancy, France), which is similar to that described in Leisen *et al.* (2012) and Lach *et al.* (2013). LA-ICPMS analyses were performed on the same fluid inclusions as those used for the microthermometry. The instrument comprises a GeoLas excimer laser (ArF, 193 nm, Microlas, Göttingen, Germany) (Günther *et al.*, 1997) and an Agilent 7500c quadrupole ICP-MS. The laser beam is focused onto the sample within a small-volume lozenge-shaped ablation cell dedicated to FI analysis using a Schwarzschild reflective objective (magnification 25x; numerical aperture 0.4) mounted on an optical microscope (Olympus BX41) equipped with an X-Y motorized stage and a CCD camera. The NIST610 glass (Jochum *et al.*, 2011) was chosen as an external standard (analytical accuracy verified with the NIST612 external standard; Longerich *et al.*, 1990). Analyses were performed under the following operating conditions: a laser fluence of 8 J/cm<sup>2</sup> and a laser shot frequency of 5 Hz; He = 0.5 L.min<sup>-1</sup> as a carrier gas mixed with Ar = 0.7 L.min<sup>-1</sup> via a cyclone mixer prior to entering the ICP torch; spot sizes of 44 µm; and an ablation duration of 40 s. The following isotopes were analyzed: <sup>7</sup>Li, <sup>23</sup>Na, <sup>24</sup>Mg, <sup>39</sup>K, <sup>43</sup>Ca (instead of <sup>40</sup>Ca to avoid interference with <sup>40</sup>Ar<sup>+</sup>), <sup>55</sup>Mn, <sup>85</sup>Rb, <sup>88</sup>Sr, <sup>89</sup>Y, <sup>93</sup>Nb, <sup>95</sup>Mo, <sup>118</sup>Sn, <sup>133</sup>Cs, <sup>138</sup>Ba, <sup>181</sup>Ta, and <sup>182</sup>W, with an integration time of 0.01 s per mass channel. These elements were selected as they were suspected to be present in the fluids based on the compositions of the successive minerals in the paragenetic successions and/or because they are usually enriched in magmatic-

hydrothermal fluids in this context (*e.g.*, Na, K, Cs, and Rb). Calibration and signal-integration were performed with the Matlab®-based SILLS program (Guillong *et al.*, 2008). Absolute element concentrations were calculated from the ratios of the analysed elements to Na. The sodium concentrations were obtained from the salinities estimated from the microthermometry analyses (in wt. % equiv. NaCl) using the charge-balance technique (Allan *et al.*, 2005). By using the analyzed elemental ratios of the major cationic species to Na, the amount of Na (as determined from the wt. % equiv. NaCl) could be corrected for contributions from other chloride salts. Each ablation spectrum was examined before further processing. Spectra were only selected if the fluid inclusion was reached after ablating the crystal surface (*e.g.* when the FI peak was completely detached from the surface contamination peak). During processing, three sectors were defined on the spectra: the background, the matrix and the FI signal. Spectra showing contamination by solid inclusions in the matrix or by crystals accidentally trapped in the FIs were discarded. A matrix correction was applied when the elements measured in the fluid inclusions were also present as trace elements in the ablated crystal. For cassiterite and fluorite-hosted inclusions, a matrix correction was applied using the SILLS program and using Sn and Ca, respectively, as internal standards (determined stoichiometrically). Consequently, Sn and Ca were not determined for fluorite- and cassiterite-hosted FIs. The matrix signal was generally constant and showed no evidence of local chemical variation. Limits of detection (LODs) were calculated using the  $3\sigma$  criterion (Longerich *et al.*, 1996). The analytical precision of most elements is within 15 % relative standard deviation (RSD). The analytical precision of the other elements is typically better than 30 % RSD (Allan *et al.*, 2005).

#### 3.4 Isotopic measurements

### 3.4.1 Oxygen isotopes of minerals and fluids

Oxygen isotope analyses of quartz, Fe-Li-micas, topaz and wolframite were carried out at the Stable Isotope Laboratory at the University of Lausanne, Switzerland, using a CO<sub>2</sub>-laser fluorination line coupled to a Finnigan MAT 253 mass spectrometer. Pure mineral separates were hand-picked under a binocular microscope and crushed in an agate mortar. For each analysis, between 1.16 and 3.15 mg of sample was loaded in the cell with the LS-1 reference material. The chamber was evacuated overnight and maintained under a vacuum better than 10<sup>-4</sup> mbar before fluorination. Samples were heated with a CO<sub>2</sub>-laser in the presence of F<sub>2</sub> and liberated oxygen gas was purified on overheated KCl salt within the extraction line. Oxygen was absorbed on a molecular sieve (13x) held at liquid nitrogen temperature, which was then heated to liberate the O<sub>2</sub> and release it into the mass spectrometer. The results for each acquisition are reported in per mil (‰) relative to VSMOW (Vienna Standard Mean Ocean Water) and are normalized to the LS-1 quartz standard (reference value: δ<sup>18</sup>O = 18.1 ‰ VSMOW). The precision, based on replicate analyses of the samples (when possible) and of the standard run with the samples, was generally better than 0.2 ‰. The values shown in Table 3 do not include replicate analyses. The oxygen isotope compositions of fluids at estimated FI trapping temperatures were calculated using the fractionation equations of Zheng (1993a) for Fe-Li-micas (lepidolite in this case), Zheng (1993b) for quartz, Zheng (1991) for wolframite, and Zheng (1993a) for topaz. The results obtained with these equations are consistent (within 0.1 ‰) with experimental calibrations in the 150–400 °C temperature range considered (wolframite: Zhang *et al.*, 1994; quartz: Sharp *et al.*, 2016). It was not possible to perform oxygen isotope analyses on cassiterite crystals because of the thin zoning.

### 3.4.2 Hydrogen isotopes of fluid inclusions



470

471 The hydrogen isotope compositions of FIs were measured at the CRPG laboratory (Nancy,  
472 France). Between 2 and 4 g of pure separates of quartz, wolframite and cassiterite were hand-  
473 picked and inserted into steel reaction vessels. Duplicates of each mineral from each deposit,  
474 were run in order to monitor the within-batch precision (*e.g.* the analytical precision). To  
475 release H<sub>2</sub>O molecules adsorbed on the mineral surface, the vessels were connected to a  
476 vacuum extraction line and heated overnight at 120 °C (Dublyansky and Spötl, 2009).  
477 Microthermometric tests were conducted before extraction to ensure that the FIs would not  
478 decrepitate nor stretch at temperatures below 200 °C. The vessels were then crushed under  
479 vacuum to release all fluids hosted in the crystals. Incondensable gases were directly removed  
480 from the extraction line so that only H<sub>2</sub>O (and possibly CO<sub>2</sub>) was collected on a liquid  
481 nitrogen cold trap. As amounts of CO<sub>2</sub> were always too low to be analyzed, CO<sub>2</sub> was  
482 therefore removed from the line. Metal reduction was chosen as the method to prepare gas  
483 samples for hydrogen isotope ratio analysis because of the small amount of sample (< 1 µl)  
484 needed (Wong *et al.*, 1984). H<sub>2</sub>O was reduced into H<sub>2</sub> by passing it through a uranium reactor  
485 heated to 800 °C (Bigeleisen *et al.*, 1952). Isotopes were analyzed using a VG 602D mass  
486 spectrometer. To ensure the accuracy of isotopic measurements, three in-house standards were  
487 also crushed and analyzed. Values of δD are reported in per mil (‰) relative to VSMOW.  
488 The same reagent was used for the reduction of consecutive water samples. Because water  
489 adheres to the internal surfaces of the uranium reactor, hydrogen isotope analyses may show a  
490 memory effect. The magnitude of this memory effect depends on the difference in the isotopic  
491 compositions and the amount of water reduced for two successive samples (Blaise *et al.*,  
492 2015). The δD values obtained from the first extraction of a sample were therefore discarded  
493 as they may have been affected by this memory effect. Isotope measurements were performed  
494 one to three times for each host mineral, depending on the amount of material available. The

deviance in  $\delta D$  between each isotopic measurement of the same sample was less than  $\pm 5 \text{ ‰}$  and was also less than the standard error.

## **4. Results**

### **4.1 Fluid inclusion petrography**

For both the Maoping and Piaotang deposits, fluid inclusions (FIs) were investigated in quartz (Fig. 7A, B, C, F, J and K), wolframite (Fig. 7E and L), cassiterite (Fig. 7D and M) and fluorite (Fig. 7G, I and N). Topaz was only investigated in the Maoping deposit (Fig. 7H). These minerals belong to pre-, syn- and post-ore stages and were used to reconstruct fluid evolution over time. Unfortunately, no FIs were found in Stages I and II minerals of the Maoping deposit. Petrographic descriptions of the FIs are summarized in Table 1. The high abundance of FIs in quartz gives the crystals a milky appearance that makes petrographic description of the FIs difficult. Other minerals contain fewer FIs and are therefore more translucent, making petrographic characterization of the FIs much easier. According to the criteria of Roedder (1984), the FIs selected in this study are either pseudosecondary (*e.g.* distributed along intragranular FI planes (FIPs)) or presumably primary (isolated, randomly distributed or clustered or aligned and/or elongated along growth zones). In all of the samples studied, there was no visible compositional difference between the pseudosecondary and the presumably primary two-phase FIs and thus these two FI types will not be further distinguished. The application of the FI assemblage (FIA) concept (Goldstein and Reynolds, 1994) is limited in this study either by the milky appearance of the quartz and/or the relatively small number of FIs over 5  $\mu\text{m}$  in size. The vast majority of FIs that were analyzed show two phases (liquid + vapor) at room temperature and typically range from 5 to 40  $\mu\text{m}$  in size. Fluid

inclusions display round, elongate, irregular or negative-crystal shapes, regardless of their location. A visual estimate of the volumetric fraction of the vapor phase relative to the entire inclusion at room temperature ( $\phi_{\text{vap}}$ ) was deduced from the area fraction of the vapor bubble at room temperature ( ) and ranged from 10 to 50 %. values are always distributed randomly in single crystals and in possible FIAs. Apparent variation in values can result, however, from two-dimensional projection of the FIs under the petrographic microscope. Any apparent variation in  $\phi_{\text{vap}}$  should therefore be considered with caution (Bakker and Diamond, 2006). Rare (< 10 %) one-phase (liquid) FIs were randomly observed in Qtz<sub>2-III</sub> and Qtz<sub>1-I</sub> from both the Maoping and the Piaotang deposits. One-phase FIs were usually either isolated or distributed randomly among two-phase FIs. One-phase and two-phase FIs show similar salinities (0.5 - 1.0 wt.% equiv. NaCl). One-phase FIs could therefore represent metastable two-phase inclusions whose bubbles had not nucleated (measured by Raman spectroscopy; Tarantola and Caumon, 2015). In addition, very rare (< 5 %) three-phase (liquid H<sub>2</sub>O + liquid CO<sub>2</sub> + vapor CO<sub>2</sub>) inclusions were observed as isolated clusters in Qtz<sub>2-III</sub> of the Maoping deposit. These three-phase aquo-carbonic inclusions were only observed in this early quartz and therefore seem to be representative of the crystallization conditions of this mineral. No apparent relationships with two-phase inclusions were identified and there was no petrographic evidence for heterogeneous trapping of different fluids within individual FIAs. The two-phase and three-phase inclusions are therefore thought to represent two distinct non-coeval fluids. Despite evidence of ductile deformation in early Qtz<sub>2-III</sub> of the Maoping deposit and Qtz<sub>1-I</sub> of the Piaotang deposit, the FIs do not show any signs of stretching or necking-down. Fluid inclusions are organized into intragranular trails that crosscut subgrain boundaries. These FIs are therefore assumed to have been unaffected by, and thus to postdate, the early quartz plastic deformation. Selected FIs do not display halos of small FIs that could reflect either decrepitation or crystal-recovery processes (Lambrecht and Diamond, 2014).

Moreover,  $\phi_{\text{vap}}$  variations observed in FIs are always randomly distributed among grains, subgrains and possible FIAs. Following the criteria of Bakker (2017) and given the descriptive features above, no evidence for post-entrapment modification of FIs due to diffusion or preferential H<sub>2</sub>O loss was identified. Cathodoluminescence imaging was used to identify any particular FI arrangements associated with textural or growth features that were not visible by optical microscope. No dark patchy halos (attributed to FIs or micropores) were observed by cathodoluminescence nor was any evidence for recrystallization found. The cathodoluminescence did however highlight the growth zoning in topaz, cassiterite and fluorite that had already been observed in transmitted light.

#### 4.2 Microthermometry

The microthermometric data of the Maoping and Piaotang FIs are summarized in Table 1 and Figure 8. The  $T_h$  and salinity data are plotted in binary diagrams for two-phase aqueous inclusions (Fig. 8).

Salinity values display a continuum in both deposits: 0.0 to 12.6 wt.% equiv. NaCl for the Maoping deposit and 0.4 to 8.3 wt.% equiv. NaCl for the Piaotang deposit. Within a single mineral, salinity varies by 2 to 8 wt.% equiv. NaCl. Two groups of  $T_h$  values can be distinguished in the two deposits: a low- $T_h$  group (150 to 250 °C) and a higher  $T_h$  group (300 to 350 °C) (Fig. 8). It was not possible to associate the observed variations in salinity and  $T_h$  with any particular petrographic feature, such as shape,  $\phi_{\text{vap}}$ , or the spatial arrangement of FIs within a crystal.

A number of similarities between the two deposits can be observed. Fluid inclusions in quartz that formed during the main mineralizing events (Qtz<sub>2-III</sub> at Maoping and Qtz<sub>1-I</sub> at Piaotang) have distinctly lower salinities than FIs in other minerals (0.0–6 wt.% equiv. NaCl), as well as

very late fluorite from both deposits have lower  $T_h$  values. Fluid inclusions in wolframite and cassiterite are characterized by high salinities (twice the salinity of quartz). At Maoping,  $Wf_{1-III}$ - and  $Cst_{1-III}$ -hosted FIs both display a narrow range of high  $T_h$ . At Piaotang,  $Cst_{1-I}$ -hosted FIs show a similarly narrow range high of  $T_h$  but the  $Wf_{1-I}$ -hosted FIs display much lower temperatures (180–230 °C) close to those of  $Qtz_{1-I}$  (150–180 °C). In late-stage minerals ( $Qtz_{4-IV}$ ,  $Fl_{1-VI}$  and  $Toz_{4-VI}$  at Maoping and  $Fl_{1-II}$  at Piaotang), salinities are generally comparable to those of cassiterite- and wolframite-hosted FIs and in the  $Qtz_{4-IV}$  at Maoping are sometimes even higher. Fluid inclusions in late-stage minerals at Maoping can be divided into two groups:  $Qtz_{4-IV}$ - and  $Fl_{2-VI}$ -hosted FIs, which display a similar range of  $T_h$  as the  $Qtz_{2-III}$  and  $Fl_{1-VI}$  FIs; and  $Toz_{4-VI}$ -hosted FIs, which, like the  $Wf_{1-III}$ - and  $Cst_{1-III}$  FIs, show a narrow range of  $T_h$ . For the aquo-carbonic FIs,  $T_m(cia)$  ranges from 7.7 to 8.1 °C and  $T_h(CO_2)$  ranges from 29.4 to 30.6 °C to the vapor phase. Total density is homogeneous among FIs (0.39 to 0.44), and compositions range from 38 to 42 %  $H_2O$  and 56 to 60 %  $CO_2$ . The total salinity of rare three-phase aquo-carbonic FIs (around 0.5 wt.% NaCl equiv.) is lower than that of most two-phase aqueous FIs.

#### 4.3 Raman spectroscopy

Raman spectroscopy data (Table 1 and Fig. 8C) were acquired from the same FIs used for microthermometry analyses. Traces of  $CO_2$ ,  $CH_4$  and  $N_2$  gases were detected by Raman spectroscopy in the vapor phase of two-phase aqueous FIs in  $Qtz_{2-III}$ ,  $Cst_{1-III}$ ,  $Qtz_{4-IV}$ ,  $Toz_{4-VI}$  in Maoping and  $Cst_{1-I}$  in Piaotang, but no associated phase transitions were observed during microthermometry analyses (Fig. 8C).

In the case of the  $Qtz_{4-IV}$  and  $Toz_{4-VI}$  FIs,  $CO_2$  was the only gas detected in the vapor phase and was present in every FI. In cassiterite and  $Qtz_{2-III}$  FIs, the gas phase showed trace but

variable amounts of CO<sub>2</sub>, CH<sub>4</sub> and N<sub>2</sub> (Fig. 8C). In the case of cassiterite, the proportions of CO<sub>2</sub>, CH<sub>4</sub> and N<sub>2</sub> varied from one FI to another but all three gases were detected in each FI. The average compositions of FI bubbles for the two deposits were 61 to 75 mol% CO<sub>2</sub>, 22 to 25 mol% CH<sub>4</sub>, and 3 to 15 mol% N<sub>2</sub> (Fig. 8C). In contrast, while CO<sub>2</sub>, CH<sub>4</sub> and N<sub>2</sub> gases were detected in the gas phase in Maoping Qtz<sub>2-III</sub> FIs, individual analyses contained none, one, two or all three of the gas species, in highly variable proportions. The FIs mainly contained bubbles filled with CO<sub>2</sub> + CH<sub>4</sub> (15 % of FIs), CH<sub>4</sub> ± N<sub>2</sub> (50 % of FIs) or pure H<sub>2</sub>O (33 % of FIs). CH<sub>4</sub> was the most frequently detected gas because of its elevated Raman cross-section. No dissolved gases were detected in the one-phase aqueous liquid FIs from the Maoping deposit.

#### 4.4 Element compositions

Two-phase aqueous FIs from the Maoping and Piaotang deposits were selected for LA-ICPMS analyses if they met the following criteria: (i) previous characterization by optical microscopy and microthermometry, (ii) relatively large in size (10-30 µm), and (iii) located an appropriate distance from the polished thick section surface (< 15 µm). From Maoping, a total of thirty-two FIs were selected from quartz (*N* = 11), cassiterite (*N* = 7), fluorite (*N* = 4) and topaz (*N* = 10). From Piaotang, a total of twenty-nine FIs were selected from quartz (*N* = 8), cassiterite (*N* = 11) and fluorite (*N* = 10). Element concentrations in FIs are reported in Table 2 and Figures 10 and 11. Since similar results were obtained for FIs in equivalent host minerals in Maoping and Piaotang, the LA-ICPMS data will hereafter be described without making any distinction between the two deposits.

Due to the relatively small size of the FIs and their relatively low salinities, data from many analyses were lower than the limit of detection (LOD). Generally speaking, LODs vary from

one analysis to another as a function of the amount of the given element in the matrix, and the ratio between the signal intensity of the inclusion and the background. In this study, the proportions of analyses above the LOD values were: Na (100%), Cs (92%), Li (90%), K (87%), Rb (85%), Mn (64%), Sn (54%), Mg (48%), W (48%), Sr (25%), Ba (25%), Mo (20%), Ta (20%), Nb (18%), Y (16%) and Ca (13%). Calcium LODs are particularly high due to analysis of the isotope  $^{43}\text{Ca}$ , which is often too low in concentration to be detected. For FIs with concentrations  $<\text{LOD}$ , the LODs show a similar range of concentrations to those measured in other inclusions from the same mineral.

In all FIs, the two main cations were Na and K, which range in concentration from 960 to 37700 ppm and from 110 to 36000 ppm, respectively. Calcium is present in high concentrations (1200 to 20000 ppm) but could only be measured in a few quartz-hosted FIs from both deposits ( $N = 8$ ).

In the Na-Li-K ternary diagram (Fig. 11A), quartz- and fluorite-hosted FIs have overlapping compositions, while cassiterite- and topaz-hosted FIs plot in two distinct fields. In Na vs. Li and Na vs. K diagrams, fluid inclusion compositions are scattered between a Na-K-Li-rich end-member (high salinity associated with cassiterite, fluorite and topaz;  $\text{Na} > 5000$  ppm,  $\text{K} > 1000$  ppm and  $\text{Li} > 100$  ppm except for one outlying value in fluorite) and a Na-K-Li-poor end-member (low-salinity associated with quartz;  $\text{Na} = 900\text{--}11000$  ppm,  $\text{K} = 900\text{--}10000$  ppm and  $\text{Li} = 10\text{--}500$  ppm) (Figs. 11B and C).

The following systematics are observed: FIs in early Qtz<sub>2-III</sub> and Qtz<sub>1-I</sub> are more depleted in Rb, Cs ( $< 150$  ppm) and Li ( $< 400$  ppm) than FIs in other minerals. The Cst<sub>1-III</sub>- and Cst<sub>1-I</sub>-hosted FIs from both deposits show the highest concentrations of Li ( $> 1600$  ppm) and Nb (15-70 ppm) as well as high amounts of Cs ( $> 400$  ppm) and W (up to 220 ppm when detected). The Fl<sub>1-VI</sub>- and Fl<sub>1-II</sub>-hosted FIs show the highest concentrations of Sr ( $> 370$  ppm). At Maoping, Qtz<sub>4-IV</sub>-hosted FIs show high Li (90-2200 ppm), Sn (120-450 ppm), W (160-300

ppm) contents and the highest concentrations of Mg and Mn (450-9900 ppm for both). Toz<sub>4-VI</sub>-hosted FIs show the highest K concentrations (> 8200 ppm) and the lowest detected Mg contents (< 120 ppm).

Fluid inclusions in quartz from both deposits have high K/Rb (20 to 420) and low Cs concentrations (< 26 ppm), while fluorite and topaz have low K/Rb and intermediate Cs contents and cassiterite has a low K/Rb (5 to 35) and high Cs content (400 to 1000 ppm; Fig. 11D).

#### 4.5 Oxygen and hydrogen stable isotopes

Oxygen and hydrogen isotopic compositions of minerals and fluids from the Maoping and Piaotang deposits are presented in Table 3 and Figure 12.

At the Maoping deposit, oxygen stable isotope analyses were performed on crystals of Fe-Li-micas<sub>2-II</sub>, Qtz<sub>2-III</sub>, Wf<sub>1-III</sub>, Cst<sub>1-III</sub>, Fe-Li-micas<sub>3-III</sub>, Qtz<sub>4-IV</sub> and Toz<sub>4-VI</sub>. At the Piaotang deposit, oxygen stable isotope analyses were performed on crystals of Qtz<sub>1-I</sub>, Wf<sub>1-I</sub> and Cst<sub>1-I</sub>. The  $\delta^{18}\text{O}$  values of Fe-Li-micas and topaz from the Maoping deposit are 8.3 - 8.7 ‰ VSMOW and 8.4 ‰ VSMOW, respectively. Quartz and wolframite from both deposits have  $\delta^{18}\text{O}$  values of 10.8 - 11.6 ‰ VSMOW and -3.0 - 0.5 ‰ VSMOW, respectively.

At the Maoping deposit, hydrogen isotope analyses were performed on FIs hosted by Qtz<sub>2-III</sub>, Wf<sub>1-III</sub>, Cst<sub>1-III</sub> and Qtz<sub>4-IV</sub>. At the Piaotang deposit, hydrogen isotope analyses were performed on FIs in Qtz<sub>1-I</sub>, Wf<sub>1-I</sub> and Cst<sub>1-I</sub> (Fig. 12B). Based on our data obtained from microthermometry and LA-ICP-MS analyses, each mineral seems to host one specific fluid composition. The  $\delta\text{D}$  values of bulk fluid inclusion contents recovered from crushing cannot therefore result from mixing of several fluid inclusion populations. All  $\delta\text{D}$  values are between -78 and -51 ‰ VSMOW. At the deposit scale,  $\delta\text{D}$  values range from -78 to -55 ‰ VSMOW



at Maoping and from -70 to -51 ‰ VSMOW at Piaotang. The following systematics are observed in both deposits:  $\delta D$  values between -59 and -51 ‰ VSMOW in fluids from Qtz<sub>2-III</sub> and Qtz<sub>1-I</sub>,  $\delta D$  values between -78 and -76 ‰ VSMOW in fluids from Wf<sub>1-III</sub> and Wf<sub>1-I</sub> and intermediate  $\delta D$  values, between -72 and -58 ‰ VSMOW, in fluids from Cst<sub>1-III</sub> and Cst<sub>1-I</sub>. In addition, fluids in the post-ore Qtz<sub>4-IV</sub> from the Maoping deposit display intermediate values, between -66 and -62 ‰ VSMOW.

## 5. Discussion

### 5.1 Identification of the fluid end-members

At both deposits, microthermometric data as well as elemental and isotopic compositions of FIs show specific fluid compositions for each host mineral and show compositional variations that point to four fluid reservoirs and mixing processes associated with successive episodes of mineral crystallization. These end-members were identified primarily from microthermometric data and then from elemental and isotopic compositions.

Variations in  $T_h$  and salinity (Figs. 8A and B) suggest a low-salinity, low-temperature end-member (**A**), an intermediate-salinity high-temperature end-member (**B**), a high-salinity high-temperature end-member (**C**), and a high-salinity low-temperature end-member (**D**). The continuum of data between the possible end-members suggests mixing trends between (**A**) and (**B**)-(**C**)-(**D**) at Maoping and between (**A**) and (**D**), and (**B**) and (**C**) at Piaotang.

End-member (**A**) is found in early quartz and fluorite from both deposits. It is characterized by low salinity (< 6 wt.% NaCl equiv.) and  $T_h$  between 100 and 250 °C (Fig. 8). Trapping conditions deduced from isochores (Fig. 9) indicate temperatures of 170 to 360 °C with associated pressures of 60 to 120 MPa, assuming hydrostatic conditions (assumed depth of

granite emplacement between 5 and 10 km). According to LA-ICPMS data, this fluid end-member is associated with low Li/Na and K/Na ratios and low Na (< 1000 ppm), Li (< 10 ppm) and K (< 100 ppm) contents. End-member (**A**) also tends to be depleted in most incompatible elements, such as Cs (< 26 ppm) and rare metals (W < 40 ppm), and displays a high K/Rb ratio of around 400. In agreement with the microthermometric and LA-ICPMS data, the stable isotope data suggest that end-member (A) is close in composition to local meteoric water. The isotopic composition of the meteoric-derived component suggested from mixing scenarios at the Xihuashan deposit, located a few kilometers away from the Maoping and Piaotang deposits, is consistent with this study (Wei *et al.*, 2012).

Fluid end-members (**B**) and (**C**) are mostly associated with the precipitation of ore minerals and define the trends in FI microthermometric data for wolframite, cassiterite, topaz and fluorite. These trends are characterized by a very narrow range of  $T_h$  (270-350 °C) that is higher than the  $T_h$  of end-member (**A**) (Fig. 8). End-members (**B**) and (**C**) are characterized by distinct salinities, with end-member (**B**) representing a low-salinity high-temperature fluid end-member (less than 2.0 wt.% equiv. NaCl) and end-member (**C**) representing a high-salinity high-temperature fluid end-member (more than 7.0 wt.% equiv. NaCl) (Fig. 8). As these variations in salinity do not significantly influence the slopes of the isochores, the trapping conditions of the two fluids are similar, with pressures similar to end-member (**A**) and temperatures between 320 and 470 °C (assuming a depth of 5–10 km and a hydrostatic gradient) (Fig. 9). Both end-members are characterized by relatively high Li/Na and K/Na ratios (> 7000, 100 and 1000 ppm for Na, Li and K respectively). Additionally, these two end-members show very low K/Rb ratios (> 50) as well as a relative enrichment in incompatible elements, such as rare metals (W > 100 ppm) and Cs (> 400 ppm), compared to end-member (**A**).

The fluid end-member (**D**) is trapped in quartz at Maoping (Qtz<sub>4-IV</sub>) and in wolframite and fluorite at Piaotang. This end-member is characterized by  $T_h$  values comparable to the Qtz<sub>1-I</sub>, Qtz<sub>2-III</sub> and Fl<sub>2-VI</sub> data that define end-member (**A**) and a salinity similar to the ore mineral FIs that characterize end-member (**C**) (Fig. 8). Fluid (**D**) was trapped at 180-380 °C and 60-120 MPa (Fig. 9). End-member (**D**) has intermediate Li/Na and K/Na ratios and moderate concentrations of incompatible elements (W, Sn, Cs, etc.) compared to end-members (**A**) and (**B**)-(C) (Fig. 11).

The hypothesis of an evolving magmatic fluid reservoir for end-members (**B**), (**C**) and (**D**) is consistent with their observed high salinities, high temperatures, and incompatible element (Li, Cs, W, etc.) contents, as well as with the trend in their isotopic compositions toward the magmatic box (Fig. 12D). Though the Maoping and Piaotang deposits do not display the higher temperatures (> 600 °C) and salinities (> 20 wt.% equiv. NaCl ) sometimes observed in magma-derived fluids (Audétat *et al.*, 2000; Webster *et al.*, 2004; Rickers *et al.*, 2006), given that the data reflect the P-T-x composition of a mixture containing meteoric fluids (end-member(A)), a magmatic origin for end-members (**B**), (**C**) and (**D**) is still consistent.

## 5.2 P-T-x evolution

In both deposits, pre-ore quartz-hosted FIs define intragranular trails and crosscut subgrain boundaries. These fluid inclusions therefore post-date the ductile deformation of quartz and could have been trapped during any post-crystallization fluid event. Furthermore, these FIs have low-salinities, contain CO<sub>2</sub>-CH<sub>4</sub>-N<sub>2</sub> gases, contain less than 400 ppm Li and less than 150 ppm Rb and Cs, and have low- $\delta D$ , *e.g.* conditions that are only seen in pre-ore quartz. Two hypotheses can therefore be put forward: (i) early quartz FI entrapment postdates quartz crystallization and deformation but predates any subsequent mineral crystallization (in this

case, wolframite and cassiterite); or (ii) early quartz FI entrapment postdates the crystallization of other minerals that did not register this event. Given that (i) the wolframite at Piaotang was deformed under the same P-T conditions as the early quartz (based on isochore interpretations), (ii) post-ore fluid stages are characterized by FIs in quartz and fluorite (minerals that can deform under the same P-T conditions as the early quartz), and (iii) none of these minerals contain FIs that show similar P-T-x conditions to the early quartz FIs, then the first hypothesis is the more likely of the two.

Crystallization of early quartz in both deposits and of wolframite in Piaotang, through mixing of the meteoric (**A**) and magmatic (**B**) (at Maoping) or (**D**) (at Piaotang) reservoirs, occurred under hydrostatic conditions (Fig. 9). The salinity resulting from this mixing ranges from essentially zero to 6 wt.% equiv. NaCl. Furthermore, wolframite and cassiterite display a higher salinity and a higher temperature. The magmatic end-member therefore seems to have become more predominant after conditions of ore crystallization were reached.

Like quartz, wolframite and cassiterite from Maoping and cassiterite from Piaotang appear to have crystallized under hydrostatic conditions (Fig. 9) and from mixing between the meteoric (**A**) and highly differentiated magmatic (**C**) reservoirs. During this stage, the temperature stabilized whereas salinity fluctuated between 5 and 12 wt.% equiv. NaCl (Fig. 8A and 8B), and the metal stock in the fluid mixture increased until saturation and the precipitation of ore minerals.

Differences between the quartz- and ore mineral-crystallizing fluids might be explained by differentiation of the granite. An increasing degree of differentiation can be traced by the decrease in the K/Rb fluid ratio (Shaw, 1968; Klemm *et al.*, 2008; Lüders *et al.*, 2009), and we observe here that the K/Rb ratio of quartz-hosted FIs is indeed significantly higher (75–414) than the ratio observed in ore-hosted FIs (7–36). Moreover, FIs in ore minerals contain higher concentrations of incompatible elements such as Cs (> 410 ppm) and rare metals such

769 as W (2 - 220 ppm, which are enriched in the residual melt during differentiation (Fig. 10 and  
770 11).

771 Quartz and ore mineral FIs also display significantly different  $\delta D$  values (-59 to -51 ‰ and -  
772 78 to -58 ‰ VSMOW, respectively). This difference cannot be explained by the  
773 differentiation process itself but some studies have demonstrated that degassing of water from  
774 the magma through fractional distillation can lead to such a decrease (Taylor *et al.*, 1983;  
775 France-Lanord *et al.*, 1988, Hedenquist and Lowenstern, 1994).

776 To confirm the validity of the processes proposed, T-x parameters were tested using the  
777 mixing proportions determined from the stable isotope contents of pre-ore quartz and ore  
778 minerals in both deposits shown in Fig. 12D. According to Fig. 12D, the proportions of  
779 mixing between the meteoric and magmatic reservoirs (expected to lie in the felsic magmatic  
780 water box) are Qtz<sub>2-III</sub> MP, 30%; Qtz<sub>1-I</sub> PT, 50%; Wf<sub>1-III</sub> MP, 25%; and Wf<sub>1-I</sub> PT, 60% (where the  
781 percentage indicates the proportion of the meteoric component).

782 For the magmatic end-member defined by the quartz FI values, the temperature would be  
783 between 260 and 500 °C, while it would be between 470 and 750 °C if the wolframite FI  
784 values were used (calculated using the minimum and maximum values determined from  
785 isochores). If we assume that the temperature of the exsolved magmatic fluid did not change  
786 over time, then the actual initial temperature must have been around 500 °C, which is  
787 consistent with current understanding (Rickers *et al.*, 2006; Thomas *et al.*, 2012; Hulsbosch *et*  
788 *al.*, 2016). Using the same dilution proportions, the magmatic end-member involved during  
789 quartz crystallization would have had a salinity of around 5 wt.% equiv. NaCl, while it would  
790 have had a salinity between 12 and 17 wt.% during wolframite crystallization. This variation  
791 can be explained by the degree of differentiation of the source (Audétat *et al.*, 2008).

792 According to the LA-ICPMS data, the quartz crystallization involved mixing of a magmatic  
793 fluid containing between 10 and 100 ppm of dissolved tungsten while during wolframite

crystallization the magmatic fluid contained around 400 ppm W (still based on the measured mixing proportions). These values are consistent with the models of Hulsbosch *et al.* (2016) for evolving tungsten contents in fluids during differentiation of the source and indicate much higher mass fractionation of the melt in the case of wolframite crystallization.

### 5.3 Regional and global implications for granite-related W-Sn deposits

FI studies have been performed on eleven W-Sn deposits from the Jiangxi and Hunan provinces in the Nanling Range and on many other W-Sn deposits worldwide (*e.g.* Norohna *et al.*, 1992; Lüders *et al.*, 2009; Ni *et al.*, 2015; Lecumberri-Sanchez *et al.*, 2017; Korges *et al.*, 2017; Fig. 13). In previous FI studies of the Maoping and Piaotang deposits, distinct microthermometric characteristics were observed in quartz- and wolframite-hosted FIs (Ni *et al.*, 2015; Chen *et al.*, 2018). While the petrographic and microthermometric data they obtained from FIs in quartz were similar to our data, both Ni *et al.* (2018) and Chen *et al.* (2018) suggested that simple cooling was the main process responsible for wolframite crystallization. Their interpretation was based on the assumption of constant salinity over time, however the salinities they report are comparable to the results of the present study (4 to 9 wt.% equiv. NaCl). Both studies invoked a magmatic and meteoric fluid, as deduced mainly from the microthermometry data, although one of the studies (Chen *et al.*, 2018) used only stable isotope data. The stable isotope data of Chen *et al.* (2018) plot between the magmatic box and the meteoric water line, but lie closer to the magmatic box than the data from this study. This difference is mainly an artefact of the temperature used to calculate the actual  $\delta^{18}\text{O}$  value of the fluid. In the case of Chen *et al.* (2018),  $\delta^{18}\text{O}$  values were calculated using  $T_h$  values without any correction for pressure, while our study used the complete range of possible temperatures determined from the isochores.

In W-Sn deposits in general, the inclusions observed are predominantly aqueous but early quartz FIs are often found to contain varying amounts of gas (CH<sub>4</sub> and N<sub>2</sub> in addition to CO<sub>2</sub>) (e.g., Norohna *et al.*, 1992; Wei *et al.*, 2012; Ni *et al.*, 2015; Chicharro *et al.*, 2016; Lecumberri-Sanchez *et al.*, 2017; Appendix A), as we observed here. In the other studies, these FIs often showed variable proportions of the vapor fraction, the presence of which could be indicative of boiling, but this was not observed in our study.

Microthermometric data from previous studies and the present study point to different trapping conditions for gangue and ore minerals (Wei *et al.*, 2012; Ni *et al.*, 2015), with higher trapping temperatures and higher salinities associated with ore fluids. Moreover, the temperatures and salinities determined in our study are similar to those found for W-Sn deposits in South China and worldwide (Fig. 13). Mineralization occurred at temperatures between 150 and 400 °C and salinities of 0 to 15 wt.% equiv. NaCl for the syn-ore fluids (Fig. 13). However, some studies show higher salinities, above 15 wt.% equiv. NaCl (e.g. Audétat *et al.*, 2000; Carruzzo *et al.*, 2000; Harlaux *et al.*, 2017). In the present study, we also demonstrate that the conditions and mixing process are maintained during post-mineralizing stages, when tungsten is still present in the fluids but is not precipitating.

Our stable isotope data (oxygen and hydrogen) are consistent with the involvement of magmatic and meteoric fluids (see Beuchat *et al.*, 2004; Carruzzo *et al.*, 2004; Wei *et al.*, 2012; Liu *et al.*, 2002; Wang *et al.*, 2012; Gong *et al.*, 2015; Feng *et al.*, 2012), which is a common interpretation despite the wide range of isotopic values reported in the literature (Fig. 12D).

The K, Rb and Cs contents of fluids indicate magma differentiation as the process responsible for generating higher W-Sn concentrations in the fluid (cf. Audétat *et al.*, 2000; Lüders *et al.*, 2009; Hulsbosch *et al.*, 2016). Recent trace element studies include Korges *et al.* (2017) and Lecumberri-Sanchez *et al.* (2017), for example. The amount of tungsten detected in our study

is comparable to that reported in the Lecumberri-Sanchez *et al.* (2017) study of the Variscan W-Sn Panasqueira deposit. However, the Korges *et al.* (2017) study was conducted on CO<sub>2</sub>-rich FIs and brines and the trace element contents cannot therefore be compared to our study due to the very distinct properties of the fluid.

Regarding the mechanism of wolframite mineralization, Lecumberri-Sanchez *et al.* (2017) and Korges *et al.* (2017) invoke a single magmatic fluid undergoing fluid-rock interaction, cooling, depressurization, and/or boiling. In the present study, temperature fluctuations are linked to variable degrees of mixing between magmatic and meteoric fluids. No depressurization or associated boiling is identified. The occasional detection of high calcium abundances in some FIs could be indicative of local fluid-rock interaction between magmatic fluids and the host rocks.

## 6. Conclusions

By combining microthermometry, Raman spectroscopy, LA-ICPMS and oxygen and hydrogen isotope analyses of fluid inclusions and their host minerals, we have been able to identify the different ore-forming processes involved in the formation of the Maoping and Piaotang W-Sn deposits in the Nanling Range in China:

- Quartz and ore minerals (wolframite and cassiterite) that precipitated during the mineralizing stages suggest mixing between a magmatic fluid exsolved from the associated peraluminous granite and a meteoric fluid. During the barren post-mineralizing stages, conditions were the same but did not lead to crystallization of ore minerals.



- The timing of ore mineral crystallization depended on the degree of differentiation of the granite. Fluids that crystallized quartz were more depleted in metals than later fluids, which were exsolved from a more differentiated melt and were enriched in incompatible elements, including metals. Quartz-forming fluids do not therefore reflect ore-forming fluids.
- In both deposits, wolframite precipitation resulted from mixing of a meteoric fluid and a highly evolved magmatic fluid. However, the mixing in each deposit occurred under different temperature conditions (350 to 450 °C at Maoping and 200 to 300 °C at Piaotang).
- Tungsten was still present in the fluid during these later stages, but did not precipitate wolframite.
- Similar mineral associations and fluid inclusion compositions are observed in all W-Sn deposits of the Nanling Range at 160-150 Ma.

## **Acknowledgements**

We are particularly grateful to Marie-Camille Caumon (Georessources, Nancy, France) for Raman spectroscopy data acquisition and Thomas Rigaudier for hydrogen isotope measurements (CRPG, Nancy, France). We would also like to thank Klaus Mezger and Marie-Camille Caumon for their editorial handling and two anonymous reviewers for their constructive comments that helped improve this article. This research was supported by the collaboration between Carnot ICEEL-Nancy and Carnot BRGM-Orléans. Access to the Maoping and Piaotang deposit and underground sampling was possible thanks to the precious help provided by Zeyang Zhu, Xudong Che, Guanglai Li, and the onsite geologists. RCW's

research is supported by the NSF of China (Grant no. 41230315), and the MOE-SAFE Affairs of China joint “111” program (Grant no. B13021).

## References

- Allan, M.M., Yardley, B.W.D., Forbes, L.J., Shmulovich, K.I., Banks, D.A., Shepherd, T.J., 2005. Validation of LA-ICP-MS fluid inclusion analysis with synthetic fluid inclusions. *American Mineralogist* 90, 1767–1775.
- Archer, D.G., 1992. Thermodynamic properties of the NaCl+H<sub>2</sub>O system. II. Thermodynamic properties of NaCl (aq), NaCl· 2H<sub>2</sub>O (cr), and phase equilibria. *Journal of Physical and Chemical Reference Data* 21, 793-829.
- Audétat, A., Günther, D., Heinrich, C.A., 2000. Magmatic-hydrothermal evolution in a fractionating granite: insights with LA-ICP-MS analysis of fluid inclusions. *Science* 279, 2091-2094.
- Audétat, A., Pettke, T., Heinrich, C.A., Bodnar, R.J., 2008. The composition of magmatic-hydrothermal fluids in barren and mineralized intrusions. *Economic Geology* 103, 877-908.
- Baker, T., Lang, J.R., 2001. Fluid inclusion characteristics of intrusion-related gold mineralization, Tombstone–Tungsten magmatic belt, Yukon Territory, Canada. *Mineralium Deposita* 36, 563-582.
- Bakker, R.J., Diamond, L.W., 2006. Estimation of volume fractions of liquid and vapor phases in fluid inclusions, and definition of inclusion shapes. *American Mineralogist* 91, 635-657.

915 Bakker, R. J., Jansen, J. B. H., 1993. Calculated fluid evolution path versus fluid inclusion  
 916 data in the COHN system as exemplified by metamorphic rocks from Rogaland, south-  
 917 west Norway. *Journal of Metamorphic Geology* 11, 357-370.

918 Bakker, R.J., 1997. Clathrates: Computer programs to calculate fluid inclusion V-X properties  
 919 using clathrate melting temperatures. *Computers & Geosciences*, 23, 1-18.

920 Bakker, R.J., 2003. Package FLUIDS 1. Computer programs for analysis of fluid inclusion  
 921 data and for modelling bulk fluid properties. *Chemical Geology* 194, 3-23.

922 Bakker, R.J., 2017. Re-equilibration processes in fluid inclusion assemblages. *Minerals* 7,  
 923 117, 1-19.

924 Ball, T.K., Fortey, N.J., Shepherd, T.J., 1985. Mineralisation at the Carrock Fell Tungsten  
 925 Mine, N. England: Paragenetic, fluid inclusion and geochemical study. *Mineralium*  
 926 *Deposita* 20, 57-65.

927 Bebout, G.E., Cooper, D.C., Bradley, A.D., Sadofsky, S.J., 1999. Nitrogen isotope record of  
 928 fluid-rock interactions in the Skiddaw aureole and granite, English Lake district.  
 929 *American Mineralogist* 84, 1495-1505.

930 Bettencourt, J.S., Leite, W.B., Goraieb, C.L., Sparrenberger, I., Bello, R.M., Payolla, B.L.,  
 931 2005. Sn-polymetallic greisen-type deposits associated with late-stage rapakivi granites,  
 932 Brazil: fluid inclusion and stable isotope characteristics. *Lithos* 80, 363-386.

933 Beuchat, S., Moritz, R., Pettke, T., 2004. Fluid evolution in the W–Cu–Zn–Pb San Cristobal  
 934 vein, Peru: fluid inclusion and stable isotope evidence. *Chemical Geology* 210, 201-  
 935 224.

936 Bigeleisen, J., Perlman, M.L., Prosser, H.C., 1952. Conversion of hydrogenic materials to  
 937 hydrogen for isotopic analysis. *Analytical Chemistry* 24, 1356-1357.

938 Blaise, T., Tarantola, A., Cathelineau, M., Boulvais, P., Techer, I., Rigaudier, T., Boiron,  
 939 M.C., Pierron, O., Landrein, P., 2015. Evolution of porewater composition through time

940 in limestone aquifers: Salinity and D/H of fluid inclusion water in authigenic minerals  
 941 (Jurassic of the eastern Paris Basin, France). *Chemical Geology* 417, 210-227.

942 Blamart, D., 1991. Les concentrations tungstifères et stannifères: caractérisation isotopique  
 943 des fluides minéralisateurs, sur l'exemple du gisement Sn-W de Walmès. Unpublished  
 944 Doctoral Thesis, INPL (Nancy, France), 167 p.

945 Bodnar, R.J., 1993. Revised equation and table for determining the freezing point depression  
 946 of H<sub>2</sub>O-NaCl solutions. *Geochimica et Cosmochimica Acta* 57, 683-684.

947 Bodnar, R.J., 2003. Introduction to aqueous-electrolyte fluid inclusions. In: Samson, I.,  
 948 Anderson, A., Marshall, D. (eds.). *Fluid Inclusions: Analysis and Interpretation*.  
 949 Mineralogical Association of Canada Short Course Series 32, 81–100.

950 Bodnar, R.J., Vityk, M.O., 1994. Interpretation of microthermometric data for H<sub>2</sub>O-NaCl  
 951 fluid inclusions. In: De Vivo, B. and Frezzotti, M.L., (eds.). *Fluid Inclusions in*  
 952 *Minerals: Methods and Application*, publisher Pontignsno-Siena, 117-130.

953 Burke, E.A., 2001. Raman microspectrometry of fluid inclusions. *Lithos* 55, 139-158.

954 Burnard, P.G., Poly, D.A. 2004. Importance of mantle derived fluids during granite  
 955 associated hydrothermal circulation: He and Ar isotopes of ore minerals from  
 956 Panasqueira. *Geochimica et Cosmochimica Acta* 68, 1607-1615.

957 Burnham, C.W., 1979. Magmas and hydrothermal fluids. In: Barnes, H.L. (eds.),  
 958 *Geochemistry of Hydrothermal ore Deposits*. John Wiley and Sons, New York, pp. 71–  
 959 136.

960 Cai, M.H., Mao, J.W., Liang, T., Pirajno, F., Huang, H.L., 2007. The origin of the Tongkeng-  
 961 Changpo tin deposit, Dachang metal district, Guanxi, China: clues from fluid inclusions  
 962 and He isotope systematics. *Mineralium Deposita* 42, 613-626.

963 Candela, P.A., 1997. A review of shallow, ore-related granites: textures, volatiles and ore  
 964 metals. *Journal of Petrology* 38, 1619–1633.

965 Cao, X. F., Lü, X. B., He, M. C., Niu, H., Du, B. F., Mei, W., 2009. An infrared microscope  
 966 investigation of fluid inclusions in coexisting quartz and wolframite: a case study of  
 967 Yaogangxian quartz-vein wolframite deposit. *Mineralium Deposita* 28, 611-620.

968 Carruzzo, S., Kontak, D.J., Clarke, D.B., 2000. Granite-hosted mineral deposits of the New  
 969 Ross area, South Mountain Batholith, Nova Scotia, Canada: P, T and X constraints of  
 970 fluids using fluid inclusion thermometry and decrepitate analysis. *Transactions of the*  
 971 *Royal Society of Edinburgh (Earth and Environmental Science)* 91, 303-319.

972 Carruzzo, S., Kontak, D.J., Clarke, D.B., Kyser, T.K., 2004. An integrated fluid–mineral  
 973 stable-isotope study of the granite-hosted mineral deposits of the New Ross area, South  
 974 Mountain Batholith, Nova Scotia, Canada: evidence for multiple reservoirs. *Canadian*  
 975 *Mineralogist* 42, 1425-1441.

976 Casanova, V., Kouzmanov, K., Audétat, A., Wälle, M., Ubrig, N., Ortelli, M., Fontboté, L.,  
 977 accepted, Fluid inclusion studies in opaque ore minerals: II. A comparative study of  
 978 synthetic fluid inclusions hosted in quartz and opaque minerals. *Economic Geology*.

979 Charoy, B. and Pollard, P.J., 1989. Albite-rich, silica-depleted metasomatic rocks at Emuford,  
 980 Northeast Queensland; mineralogical, geochemical, and fluid inclusion constraints on  
 981 hydrothermal evolution and tin mineralization. *Economic Geology* 84, 1850-1874.

982 Charvet, J., 2013. The Neoproterozoic-Early Paleozoic tectonic evolution of the South China  
 983 Block: an overview. *Journal of Asian Earth Sciences* 74, 198-209.

984 Charvet, J., Shu, L-S., Faure, M., Choulet, F., Wang, B., Lu, H-F., Le Breton, N., 2010.  
 985 Structural development of the Lower Palaeozoic belt of South China: genesis of an  
 986 intracontinental orogeny. *Journal of Asian Earth Sciences* 39, 309-330.

987 Chen, L.L., Ni, P., Li, W.S., Ding, J.Y., Pan, J.Y., Wang, G.G., Yang, Y.L., 2018. The link  
 988 between fluid evolution and vertical zonation at the Maoping tungsten deposit, Southern

989 Jiangxi, China: Fluid inclusion and stable isotope evidence. *Journal of Geochemical*  
990 *Exploration* 192, 18-32.

991 Chicharro, E., Boiron, M. C., López-García, J. Á., Barfod, D. N., Villaseca, C., 2016. Origin,  
992 ore forming fluid evolution and timing of the Logrosán Sn–(W) ore deposits (Central  
993 Iberian Zone, Spain). *Ore Geology Reviews* 72, 896-913.

994 Davis, W.J. and Williams-Jones, A.E., 1985. A fluid inclusion study of the porphyry-greisen,  
995 tungsten-molybdenum deposit at Mount Pleasant, New Brunswick, Canada. *Mineralium*  
996 *Deposita* 20, 94-101.

997 Deen, J.A., Rye, R.O., Munoz, J.L., Drexler, J.W., 1994. The magmatic hydrothermal system  
998 at Julcani, Peru; evidence from fluid inclusions and hydrogen and oxygen isotopes.  
999 *Economic Geology* 89, 1924-1938.

1000 Dewaele, S., De Clercq, F., Hulsbosch, N., Piessens, K., Boyce, A., Burgess, R., Muchez, P.,  
1001 2016. Genesis of the vein-type tungsten mineralization at Nyakabingo (Rwanda) in the  
1002 Karagwe–Ankole belt, Central Africa. *Mineralium Deposita* 51, 283-307.

1003 Dolníček, Z., René, M., Prochaska, W., Kovář, M., 2012. Fluid evolution of the Hub Stock,  
1004 Horní Slavkov–Krásno Sn–W ore district, Bohemian Massif, Czech Republic.  
1005 *Mineralium Deposita* 47, 821-833.

1006 Duan, Z., Møller, N., Weare, J.H., 1995. Equation of state for the NaCl-H<sub>2</sub>O-CO<sub>2</sub> system:  
1007 prediction of phase equilibria and volumetric properties. *Geochimica et Cosmochimica*  
1008 *Acta* 59, 2869-2882.

1009 Dublyansky, Y. V., Spötl, C., 2009. Hydrogen and oxygen isotopes of water from inclusions  
1010 in minerals: design of a new crushing system and on-line continuous-flow isotope ratio  
1011 mass spectrometric analysis. *Rapid Communications in Mass Spectrometry* 23, 2605-  
1012 2613.

1013 Feng, C., Zeng, Z., Zhang, D., Qu, W., Du, A., Li, D., She, H., 2011. SHRIMP zircon U–Pb  
1014 and molybdenite Re–Os isotopic dating of the tungsten deposits in the Tianmenshan–  
1015 Hongtaoling W–Sn orefield, southern Jiangxi province, China, and geological  
1016 implications. *Ore Geology Reviews* 43, 8-25.

1017 Feng, C.Y., Wang, S., Zeng, Z.L., Zhang, D.H., Li, D.X., She, H.Q., 2012. Fluid inclusion  
1018 and chronology studies of Baxiannao mineralized fractured zone-type tungsten  
1019 polymetallic deposit, southern Jiangxi province, China. *Acta Petrologica Sinica* 28, 52-  
1020 64 (in Chinese with English abstract).

1021 France-Lanord, C., Sheppard, S.M., Le Fort, P., 1988. Hydrogen and oxygen isotope  
1022 variations in the High Himalaya peraluminous Manaslu leucogranite: evidence for  
1023 heterogeneous sedimentary source. *Geochimica et Cosmochimica Acta* 52, 513-526.

1024 Giuliani, G., Li, Y.D., Sheng, T.F., 1988. Fluid inclusion study of Xihuashan tungsten deposit  
1025 in the southern Jiangxi province, China. *Mineralium Deposita* 23, 24–33.

1026 Goldstein, R.H. and Reynolds, T.J., 1994. Systematics of fluid inclusions in diagenetic  
1027 minerals. *Society for sedimentary geology Short Course* 31, 199 p.

1028 Gong, X. D., Yan, G. S., Ye, T. Z., Zhu, X. Y., Li, Y. S., Zhang, Z. H., Jia, W. B., Yao, X. F.,  
1029 2015. A study of ore-forming fluids in the Shimensi Tungsten Deposit, Dahutang  
1030 Tungsten Polymetallic Ore Field, Jiangxi province, China. *Acta Geologica Sinica* 89,  
1031 822-835.

1032 Graupner, T., Kempe, U., Dombon, E., Pätzold, O., Leeder, O., Spooner, E.T.C., 1999. Fluid  
1033 regime and ore formation in the tungsten (–yttrium) deposits of Kyzyltau (Mongolian  
1034 Altai): evidence for fluid variability in tungsten–tin ore systems. *Chemical Geology*  
1035 154, 21-58.

1036 Guillong, M., Meier, D.L., Allan, M., Heinrich, C.A., Yardley, B.W.D., 2008. SILLS: A  
1037 Matlab-based program for the reduction of laser ablation ICP-MS data of homogeneous

1038 materials and inclusions. In: Sylvester P (eds.). Laser Ablation ICP–MS in the Earth  
 1039 Sciences: Current Practices and Outstanding Issues. Mineralogical Association of  
 1040 Canada Short Course Series 40, 328–333.

1041 Günther, D., Frischknecht, R., Heinrich, C.A., Kahlert, H.J., 1997. Capabilities of an Argon  
 1042 Fluoride 193 nm Excimer laser for laser ablation inductively coupled plasma mass  
 1043 spectrometry microanalysis of geological materials. *Journal of Analytical Atomic*  
 1044 *Spectrometry* 12, 939-944.

1045 Guo, C., Chen, Y., Zeng, Z., Lou, F., 2012. Petrogenesis of the Xihuashan granites in  
 1046 southeastern China: Constraints from geochemistry and in-situ analyses of zircon U-Pb-  
 1047 Hf-O isotopes. *Lithos* 148, 209-227.

1048 Harlaux, M., Mercadier, J., Bonzi, W.M.E., Kremer, V., Marignac, C., Cuney, M., 2017.  
 1049 Geochemical Signature of Magmatic-Hydrothermal Fluids Exsolved from the Beauvoir  
 1050 Rare-Metal Granite (Massif Central, France): Insights from LA-ICPMS Analysis of  
 1051 Primary Fluid Inclusions. 2017. *Geofluids*, Article ID 1925817.

1052 Hedenquist, J.W. and Lowenstern, J.B., 1994. The role of magmas in the formation of  
 1053 hydrothermal ore deposits. *Nature* 370, 519.

1054 Higgins, N.C., 1985. Wolframite deposition in a hydrothermal vein system; the Grey River  
 1055 tungsten prospect, Newfoundland, Canada. *Economic Geology* 80, 1297-1327.

1056 Hoffmann, C.F., Henley, R.W., Higgins, N.C., Solomon, M., Summons, R.E., 1988. Biogenic  
 1057 hydrocarbons in fluid inclusions from the Aberfoyle tin-tungsten deposit, Tasmania,  
 1058 Australia. *Chemical Geology* 70, 287-299.

1059 Hu, R.Z., Bi, X.W., Jiang, G.H., Chen, H.W., Peng, J.T., Qi, Y.Q., Wu, L.Y., Wei, W.F.,  
 1060 2012. Mantle-derived noble gases in ore-forming fluids of the granite-related  
 1061 Yaogangxian tungsten deposit, Southeastern China. *Mineralium Deposita* 47, 623-632.



- 1062 Hua, R., Chen, P., Zhang, W., Lu, J., 2005. Three large-scale metallogenic events related to  
1063 the Yanshanian Period in Southern China. Edition: Mineral Deposit Research: Meeting  
1064 the Global Challenge. Springer Berlin, Heidelberg, 401-404.
- 1065 Hulsbosch, N., Boiron, M.C., Dewaele, S., Muchez, P., 2016. Fluid fractionation of tungsten  
1066 during granite–pegmatite differentiation and the metal source of peribatholithic W quartz  
1067 veins: Evidence from the Karagwe-Ankole Belt (Rwanda). *Geochimica et*  
1068 *Cosmochimica Acta* 175, 299-318.
- 1069 Jochum, K.P., Weis, U., Stoll, B., Kuzmin, D., Yang, Q., Raczek, I., Jacob, D.E., Stracke, A.,  
1070 Birbaum, K., Frick, D.A., Gunther, D.,ENZWEILER, J., 2011. Determination of reference  
1071 values for NIST SRM 610-617 glasses following ISO guidelines. *Geostandards and*  
1072 *Geoanalytical Research* 35, 397-429.
- 1073 Joyce, D.B. and Voigt, D.E., 1994. A phase equilibrium study in the system  $\text{KAlSi}_3\text{O}_8$ -  
1074  $\text{NaAlSi}_3\text{O}_8$ - $\text{SiO}_2$ - $\text{Al}_2\text{SiO}_5$ - $\text{H}_2\text{O}$  and petrogenetic implications. *American Mineralogist*  
1075 79, 504-512.
- 1076 Kamenetsky, V.S., Naumov, V.B., Davidson, P., van Achtenbergh, E., Ryan, C.G., 2004.  
1077 Immiscibility between silicate magmas and aqueous fluids: a melt inclusion pursuit into  
1078 the magmatic-hydrothermal transition in the Omsukchan Granite (NE Russia). *Chemical*  
1079 *Geology* 210, 73-90.
- 1080 Klemm, L. M., Pettke, T., Heinrich, C. A., 2008. Fluid and source magma evolution of the  
1081 Questa porphyry Mo deposit, New Mexico, USA. *Mineralium Deposita*, 43, 533.
- 1082 Korges, M., Weis, P., Lüders, V., Laurent, O., 2017. Depressurization and boiling of a single  
1083 magmatic fluid as a mechanism for tin-tungsten deposit formation. *Geology* 46, 75-78.
- 1084 Krylova, T.L., Pandian, M.S., Bortnikov, N.S., Gorelikova, N.V., Gonevchuk, V.G.,  
1085 Korostelev, P.G., 2012. Degana (Rajasthan, India) and Tigrinoe (Primorye, Russia)

1086 tungsten and tin-tungsten deposits: Composition of mineral-forming fluids and  
 1087 conditions of wolframite deposition. *Geology of Ore Deposits* 54, 276-294.

1088 Lach, P., Mercadier, J., Dubessy, J., Boiron, M.C., Cuney, M., 2013. In situ quantitative  
 1089 measurement of rare earth elements in uranium oxides by laser ablation-inductively  
 1090 coupled plasma-mass spectrometry. *Geostandards and Geoanalytical Results* 37, 1-20.

1091 Lambrecht, G., and Diamond, L.W., 2014. Morphological ripening of fluid inclusions and  
 1092 coupled zone-refining in quartz crystals revealed by cathodoluminescence imaging:  
 1093 Implications for CL-petrography, fluid inclusion analysis and trace-element  
 1094 geothermometry. *Geochimica et Cosmochimica Acta* 141, 381-406.

1095 Landis, G.P. and Rye, R.O., 1974. Geologic, fluid inclusion, and stable isotope studies of the  
 1096 Pasto Buena tungsten-base metal ore deposit, Northern Peru. *Economic Geology* 69,  
 1097 1025-1059.

1098 Lecumberri-Sanchez, P., Vieira, R., Heinrich, C.A., Pinto, F., Wälle, M., 2017. Fluid-rock  
 1099 interaction is decisive for the formation of tungsten deposits. *Geology* 45, 579-582.

1100 Legros, H., Marignac, C., Mercadier, J., Cuney, M., Richard, A., Wang, R-C., Charles, N.,  
 1101 Lespinasse, M-Y., 2016. Detailed paragenesis and Li-mica compositions as recorders of  
 1102 the magmatic-hydrothermal evolution of the Maoping W-Sn deposit (Jiangxi, China).  
 1103 *Lithos* 264, 108-124.

1104 Legros, H., Marignac, C., Tabary, T., Mercadier, J., Richard, A., Cuney, M., Wang, R-C.,  
 1105 Charles, N., Lespinasse, M-Y., 2018. The ore-forming magmatic-hydrothermal system  
 1106 of the Piaotang W-Sn deposit (Jiangxi, China) as seen from Li-mica geochemistry.  
 1107 *American Mineralogist* 103, 39-54.

1108 Leisen, M., Boiron, M.C., Richard, A., Dubessy, J., 2012. Determination of Cl and Br  
 1109 concentrations in individual fluid inclusions by combining microthermometry and LA-

1110 ICPMS analysis: Implications for the origin of salinity in crustal fluids. *Chemical*  
 1111 *Geology* 330-331, 197-206.

1112 Li, Z-X., Qiu, J-S., Yang, X-M., 2014. A review of the geochronology and geochemistry of  
 1113 Late Yanshanian (Cretaceous) plutons along the Fujian coastal area of southeastern  
 1114 China: Implications for magma evolution related to slab break-off and rollback in the  
 1115 Cretaceous. *Earth-Science Reviews* 128, 232–248.

1116 Li, Z-X., Wartho, J-A., Occhipinti, S., Zhang, C-L., Li, X-H., Wang, J., Bao, C-M., 2007.  
 1117 Early history of the eastern Sibao Orogen (South China) during the assembly of  
 1118 Rodinia: new mica  $^{40}\text{Ar}/^{39}\text{Ar}$  dating and SHRIMP U-PB detrital zircon provenance  
 1119 constraints. *Precambrian Research* 159, 79-94.

1120 Liu, J.Q., Wang, X.W., Zeng, Y.S., Wang, X.D., 2002. Xihuashan granite and evolution of  
 1121 ore-forming fluid of tungsten-tin-beryllium ore field. *Geology and Mineral Resources of*  
 1122 *South China* 3, 91-96.

1123 Longerich, H.P., Jenner, G.A., Fryer, B.J., Jackson, S.E., 1990. Inductively coupled plasma-  
 1124 mass spectrometric analysis of geological samples: a critical evaluation based on case  
 1125 studies. *Chemical Geology* 83, 105-118.

1126 Longerich, H.P., Jackson, S.E., Günther, D., 1996. Laser ablation inductively coupled plasma  
 1127 mass spectrometric transient signal data acquisition and analyte concentration  
 1128 calculation. *Journal of Analytical Atomic Spectrometry* 11, 899-904.

1129 Lüders, V., Romer, R. L., Gilg, H. A., Bodnar, R. J., Pettke, T., Misantoni, D., 2009. A  
 1130 geochemical study of the Sweet Home Mine, Colorado Mineral Belt, USA:  
 1131 hydrothermal fluid evolution above a hypothesized granite cupola. *Mineralium*  
 1132 *Deposita*, 44, 415.

- 1133 Macey, P. and Harris, C., 2006. Stable isotope and fluid inclusion evidence for the origin of  
1134 the Brandberg West area Sn–W vein deposits, NW Namibia. *Mineralium Deposita* 41,  
1135 671-690.
- 1136 Mao, J.W., Xie, G.Q., Guo, C.L., Chen, Y.C., 2007. Large-scale tungsten–tin mineralization  
1137 in the Nanling region, South China: metallogenic ages and corresponding geodynamic  
1138 processes. *Acta Petrologica Sinica* 23, 2329-2338 (in Chinese with English abstract).
- 1139 Mao, X-L., Wang, Q., Liu, S., Xu, M., Wang, L., 2012. Effective elastic thickness and  
1140 mechanical anisotropy of South China and surrounding regions. *Tectonophysics* 550-  
1141 553, 47–56.
- 1142 Marignac, C. and Cathelineau, M., 2009. The nature of ore-forming fluids in peri-batholithic  
1143 Sn-W deposits and a classification. In: Williams *et al.* (eds.). *Smart science for*  
1144 *exploration and mining*, Proceedings 10th Biennial SGA Meeting, Townsville: 245-247.
- 1145 Mishra, B., Pal, D.C., Panigrahi, M.K., 1999. Fluid evolution in quartz vein-hosted tungsten  
1146 mineralization in Chhendapathar, Bankura District, West Bengal: Evidence from fluid  
1147 inclusion study. *Proceedings of the Indian Academy of Sciences-Earth and Planetary*  
1148 *Sciences* 108, 23-31.
- 1149 Morishita, Y., 1991. Fluid evolution and geobarometry on the Ohtani and Kaneuchi tungsten-  
1150 quartz vein deposits, Japan: oxygen and carbon isotopic evidence. *Mineralium Deposita*  
1151 26, 40-50.
- 1152 Moritz, R., 2006. Fluid salinities obtained by infrared microthermometry of opaque minerals:  
1153 Implications for ore deposit modeling—a note of caution. *Journal of Geochemical*  
1154 *Exploration* 89, 284-287.
- 1155 Moura, A., Dória, A., Neiva, A.M.R., Gomes, C.L., Creaser, R.A., 2014. Metallogenesis at  
1156 the Carris W–Mo–Sn deposit (Gerês, Portugal): constraints from fluid inclusions,  
1157 mineral geochemistry, Re–Os and He–Ar isotopes. *Ore Geology Reviews* 56, 73-93.

1158 Ni, P., Wang, X.D., Wang, G.G., Huang, J.B., Pan, J.Y., Wang, T.G., 2015. An infrared  
1159 microthermometric study of fluid inclusions in coexisting quartz and wolframite from  
1160 Late Mesozoic tungsten deposits in the Gannan metallogenic belt, South China. *Ore*  
1161 *Geological Reviews* 65, 1062-1077.

1162 Noronha, F., Doria, A., Dubessy, J., Charoy, B., 1992. Characterization and timing of the  
1163 different types of fluids present in the barren and ore veins of the W-Sn deposit of  
1164 Panasqueira, Central Portugal. *Mineralium Deposita* 27, 72-79.

1165 Ortellì, M., Kouzmanov, K., Wälle, M., Ubrig, N., Casanova, V., accepted, Fluid inclusion  
1166 studies in opaque ore minerals: I. Trace element content and physical properties of ore  
1167 minerals controlling textural features in transmitted near-infrared light microscopy.  
1168 *Economic Geology*.

1169 Pirajno, F., 2009. *Hydrothermal Processes and Mineral Systems*. Springer, Dordrecht, 1250 p.

1170 Pohl, W. and Günther, M.A., 1991. The origin of Kibaran (late Mid-Proterozoic) tin, tungsten  
1171 and gold quartz vein deposits in Central Africa: a fluid inclusions study. *Mineralium*  
1172 *Deposita* 26, 51-59.

1173 Polya, D.A., Foxford, K.A., Stuart, F., Boyce, A., Fallick, A.E., 2000. Evolution and  
1174 paragenetic context of low  $\delta D$  hydrothermal fluids from the Panasqueira W-Sn deposit,  
1175 Portugal: New evidence from microthermometric, stable isotope, noble gas and halogen  
1176 analyses of primary fluid inclusions. *Geochimica et Cosmochimica Acta* 64, 3357-3371.

1177 Rickers, K., Thomas, R., Heinrich, W., 2006. The behavior of trace elements during the  
1178 chemical evolution of the H<sub>2</sub>O-, B-, and F-rich granite-pegmatite-hydrothermal system  
1179 at Ehrenfriedensdorf, Germany: a SXRF study of melt and fluid inclusions. *Mineralium*  
1180 *Deposita* 41, 229-245.

1181 Roedder, E., 1984. Fluid Inclusions. *Reviews in Mineralogy* 12, 644 p.

1182 Schrötter, H.W., and Klöckner, H.W., 1979. Raman scattering cross sections in gases and  
 1183 liquids. In: Weber A. (eds.) Raman Spectroscopy of Gases and Liquids. Topics in  
 1184 Current Physics, vol 11. Springer, Berlin, Heidelberg.

1185 Sharp, Z.D., Gibbons, J.A., Maltsev, O., Atudorei, V., Pack, A., Sengupta, S., Schock, E.L.,  
 1186 Knauth, L. P., 2016. A calibration of the triple oxygen isotope fractionation in the SiO<sub>2</sub>–  
 1187 H<sub>2</sub>O system and applications to natural samples. *Geochimica et Cosmochimica Acta*  
 1188 186, 105-119.

1189 Shaw, D. M., 1968. A review of K-Rb fractionation trends by covariance analysis.  
 1190 *Geochimica et Cosmochimica Acta*, 32, 573-601.

1191 Sheppard, S.M.F., 1994. Stable isotope and fluid inclusion evidence for the origin and  
 1192 evolution of Hercynian mineralizing fluids. In: Seltmann, R., Kämpf, H., Möller, P.  
 1193 (eds.) *Metallogeny of collisional orogens*. Czech Geological Survey, Prague, pp. 49-60.

1194 Smith, M., Banks, D.A., Yardley, B.W.D., Boyce, A., 1996. Fluid inclusion and stable isotope  
 1195 constraints on the genesis of the Cligga Head Sn-W deposit, S.W. England. *European*  
 1196 *Journal of Mineralogy* 8, 961-974.

1197 So, C.S., and Yun, S.T., 1994. Origin and evolution of W-Mo-producing fluids in a granitic  
 1198 hydrothermal system; geochemical studies of quartz vein deposits around the Susan  
 1199 Granite, Hwanggangri District, Republic of Korea. *Economic Geology* 89, 246-267.

1200 Sun, W.D., Yang, X.Y., Fan, W.M., Wu, F.Y., 2012. Mesozoic large scale magmatism and  
 1201 mineralization in South China: preface. *Lithos* 150, 1-5.

1202 Tarantola, A. and Caumon, M.C., 2015. Raman spectra of water in fluid inclusions: II. Effect  
 1203 of negative pressure on salinity measurement. *Journal of Raman Spectroscopy* 46, 977-  
 1204 982.

1205 Taylor, B.E., Eichelberger, J.C., Westrich, H.R., 1983. Hydrogen isotopic evidence of  
 1206 rhyolitic magma degassing during shallow intrusion and eruption. *Nature* 306, 541-545.

1207 Thomas, R., Förster, H.J., Rickers, K., Webster, J., 2005. Formation of extremely F-rich  
1208 hydrous melt fractions and hydrothermal fluids during differentiation of highly evolved  
1209 tin-granite magmas: a melt-fluid inclusion study. *Contributions to Mineralogy and*  
1210 *Petrology* 148, 582-641.

1211 Thomas R., Davidson P., Beurlen H., 2012. The competing models for the origin and internal  
1212 evolution of granitic pegmatites in the light of melt and fluid inclusion research.  
1213 *Mineralogy and Petrology* 106, 55–73.

1214 USGS, 2017. Tungsten. *Mineral Commodity Summaries*, p. 180-181.

1215 Vindel, E., Lopez, J.A., Boiron, M-C., Cathelineau, M., Prieto, A.C., 1995. *PV-T-X-fO<sub>2</sub>*  
1216 evolution from wolframite to sulphide depositional stage in intragranitic W-veins. An  
1217 example from the Spanish Central System. *European Journal of Mineralogy* 7, 675-688.

1218 Wang, Z.Q., Yin, C.Y., Gao, L.Z., Tang, F., Liu, Y.Q., Liu, P.J., 2006. The character of the  
1219 chemical index of alteration and discussion of subdivision and correlation of the Nanhua  
1220 System in Yichang area. *Geological Review* 52, 577-585.

1221 Wang, X-D., Ni, P., Jiang, S-Y., Zhao, K-D., Wang, T-G., 2009. Origin of ore-forming fluid  
1222 in the Piaotang tungsten deposit in Jiangxi province: Evidence from helium and argon  
1223 isotopes. *Chinese Science Bulletin* 55, 628-634.

1224 Wang, Q.Y., Lu, Y.F., Chen, Z.H., Peng, X.L., Xiong, X.F., 2012. Fluid inclusion  
1225 characteristic and its geological implication of the Taoxikeng tungsten deposit, southern  
1226 Jiangxi province. *Geology and Mineral Resources of South China* 1, 006.

1227 Wang, Y-J., Fan, W-M., Zhang, G-W., Zhang, Y-H., 2013. Phanerozoic tectonics of the South  
1228 China Block: key observations and controversies. *Gondwana Research* 23, 1273-1305.

1229 Webster, J.D., Thomas, R., Förster, H.J., Seltmann, R., Tappen, C., 2004. Geochemical  
1230 evolution of halogen-enriched, granite magmas and mineralising fluids of the Zinnwald  
1231 tin-tungsten mining district, Erzgebirge, Germany. *Mineralium Deposita* 39, 452-472.

- 1232 Wei, W., Hu, R., Bi, X., Peng, J., Su, W., Song, S., Shi, S., 2012. Infrared microthermometric  
1233 and stable isotopic study of fluid inclusions in wolframite at the Xihuashan tungsten  
1234 deposit, Jiangxi province, China. *Mineralium Deposita* 47, 589-605.
- 1235 Wei, W-F., Yan, B., Shen, N-P., Liu, L., Zhang, Y., Xiang, X-K., 2017. Muscovite  $^{40}\text{Ar}/^{39}\text{Ar}$   
1236 age and H-O-S isotopes of the Shimenshi tungsten deposit (Northern Jiangxi province,  
1237 South China) and their metallogenic implications. *Minerals* 7, 162.
- 1238 Weisbrod, A., 1988. Caractères généraux des phases fluides dans les indices et gisements de  
1239 tungstène et d'étain. In: Johan, Z., Ohnenstetter, D., (eds.), *Gisements métallifères dans*  
1240 *leur contexte géologique*, Documents du BRGM 158-1, 9-14.
- 1241 Wilkinson, J.J., 1990. The role of metamorphic fluids in the development of the Cornubian  
1242 Orefield: fluid inclusion evidence from south Cornwall. *Mineralogical Magazine* 54,  
1243 219-230.
- 1244 Wilkinson, J.J., 2001. Fluid inclusions in hydrothermal ore deposits. *Lithos* 55, 229-272.
- 1245 Wong, W.W., Cabreara, M.P., Klein, P.D., 1984. Evaluation of a dual mass spectrometer  
1246 system for rapid simultaneous determination of hydrogen-2/hydrogen-1 and oxygen-  
1247 18/oxygen-16 ratios in aqueous samples. *Analytical Chemistry* 56, 1852–1858.
- 1248 Xi, B.B., Zhang, D.H., Zhou, L.M., 2007. Magmatic evolutions of several granite plutons  
1249 related to Sn (W) mineralization in the Nanling region, China. *Geological Bulletin*  
1250 *China* 26, 1591-1599 (in Chinese with English abstract).
- 1251 Xi, B., Zhang, D., Zhou, L., Zhang, W., Wang, C., 2008. Characteristics of ore forming fluid  
1252 evolution in Dajishan Tungsten Deposit, Quannan County, Jiangxi. *Acta Geologica*  
1253 *Sinica* 82, 956-966.
- 1254 Xiong, Y.Q., Shao, Y.J., Zhou, H.D., Wu, Q.H., Liu, J.P., Wei, H.T., Zhao, R.C., Cao, J.Y.,  
1255 2017. Ore-forming mechanism of quartz-vein-type W-Sn deposits of the Xitian district



1256 in SE China: Implications from the trace element analysis of wolframite and  
 1257 investigation of fluid inclusions. *Ore Geology Reviews* 83, 152-173.

1258 Xuexin, S., Jingkai, Z., 1990. Study of fluid inclusions of the Shizhuyuan-Yejiwei W-Sn-Mo-  
 1259 Bi-polymetallic deposit in southern Hunan. *Mineral Deposits* 4, 004.

1260 Yoo, B., Lee, H., White, N., 2010. Mineralogical, fluid inclusion, and stable isotope  
 1261 constraints on mechanisms of ore deposition at the Samgwang mine (Republic of  
 1262 Korea) - a mesothermal, vein-hosted gold–silver deposit. *Mineralium Deposita* 45, 161-  
 1263 187.

1264 Zaw, K., Peters, S. G., Cromie, P., Burrett, C., Hou, Z., 2007. Nature, diversity of deposit  
 1265 types and metallogenic relations of South China. *Ore Geology Reviews* 31, 3-47.

1266 Zeng, Y., Liu, J., Zhu, Y., 2002. Short-chain carboxylates in high-temperature ore fluids of  
 1267 W-Sn deposits in south China. *Geochemical Journal* 36, 219-234.

1268 Zeng, Z.L., Zhu, X.P., Xu, J.X., 2007. Tungsten Reserves of Southern Jiangxi province and  
 1269 Prospecting Outlook. *China Tungsten Industry* 6, 16-24 (in Chinese with English  
 1270 abstract).

1271 Zhang L.-G., Liu J.-X., Chen Z.-S., Zhou H.B., 1994. Experimental investigations of oxygen  
 1272 isotope fractionation in cassiterite and wolframite. *Economic Geology* 89, 150-157.

1273 Zhang, D.Q., Feng, C.Y., Li, D.X., Chen, Y.C., Zeng, Z.L., 2012. Fluid Inclusions  
 1274 Characteristics and Ore Genesis of Taoxikeng Tungsten and Tin Deposit in Chongyi  
 1275 County, Jiangxi province. *Journal of Jilin University (Earth Science Edition)* 42, 374-  
 1276 383.

1277 Zhang, R., Lu, J., Lehmann, B., Li, C., Li, G., Zhang, L., Sun, W., 2017. Combined zircon  
 1278 and cassiterite U–Pb dating of the Piaotang granite-related tungsten–tin deposit,  
 1279 southern Jiangxi tungsten district, China. *Ore Geology Reviews* 82, 268-284.

Zheng, Y.F., 1991. Calculation of oxygen isotope fractionation in metal oxides. *Geochimica et Cosmochimica Acta* 55, 2299-2307.

Zheng, Y. F., 1993a. Calculation of oxygen isotope fractionation in hydroxyl-bearing silicates. *Earth and Planetary Science Letters* 120, 247-263.

Zheng, Y.F., 1993b. Calculation of oxygen isotope fractionation in anhydrous silicate minerals. *Geochimica et Cosmochimica Acta* 57, 1079-1079.

Zhou, Y.Z., Gao, C.S., Hong, Y.L., Han, Z.X., Wen, L.H., 2010. Diagenesis-mineralization process and mineralization models of Xihuashan granite. *China Tungsten Industry* 25, 12-1 (in Chinese with English abstract).

#### **Figure captions**

Figure 1: Geological and geographical context of the Maoping and Piaotang deposits (modified after Legros *et al.*, 2016). (A) Locations of mineral deposits and Cretaceous and Jurassic granitoids of the Cathaysia Block. Most W-Sn deposits from the Cathaysia Block are located in the Nanling Metallogenic Belt, here indicated in orange, and associated with Jurassic and Cretaceous granitoids. The southern Jiangxi Province is outlined in red (B) Location of mining districts, associated mineral deposits and Cretaceous and Jurassic granitoids from the southern part of the Southern Jiangxi province. The Southern Jiangxi province is the richest part of the Nanling Metallogenic Belt in terms of W-Sn resources. The Maoping and Piaotang deposits are located in the Dayu district in the western part of the Southern Jiangxi province.

Figure 2: Location, schematic cross-sections and sampling levels of the studied deposits showing the relationships between the deep Jurassic granites, Cambrian host rocks, and W-Sn quartz veins. (A) and (B) Maoping deposit (Modified after Feng *et al.*, 2011 and Legros *et al.*, 2016), located near the Tiangmenshan granite. The Maoping granite is thought to be the north-plunging extension of this granite (Feng *et al.*, 2011). (C) and (D) Piaotang deposit (Modified after Ni *et al.*, 2015 and Legros *et al.*, 2017), located near the Xihuashan deposit. Like the Maoping deposit, the Piaotang deposit also exhibits a greisen cupola in the field but it could not be defined well enough in this study to modify the cross-section of Ni *et al.*, (2015).

Figure 3: Paragenetic sequence of the Maoping W-Sn deposit based on samples from the mine gallery at level -5 (e.g. -200 m; the only level drawn on the cross-section in Fig. 2A) modified after Legros *et al.* (2016). Details of the different stages and petrographic descriptions are provided in Legros *et al.* (2016). Minerals indicated in color (here, quartz, wolframite, cassiterite, fluorite and topaz) were chosen for this FI study. Colors are in accordance with Figures 8 to 12.

Figure 4: Textural characterization of minerals from the Maoping deposit selected for FI study, according to their respective stages. Modified after Legros *et al.* (2016). (A) W-Sn vein (Stage III). (B) Association of Qtz<sub>2-III</sub> with Cst<sub>1-III</sub> and Fe-Li-mca<sub>3-III</sub> (Stage III) (cross polars). (C) Complex growth-zones in the Mn-rich wolframite Wf<sub>1-III</sub> (Stage III) (natural light). (D) Complex growth zones in cassiterite Cst<sub>1-III</sub> of stage III (natural light). (E) Banded quartz vein (Stage IV) showing the centimeter-scale banding of quartz and Fe-Li-micas. (F) Stage IV banded quartz (thick section observed under crossed polars). (G) Two generations of fluorite (Fl<sub>1-VI</sub> and Fl<sub>2-VI</sub>)

from Stage VI (observed by cathodoluminescence). (H) Overgrowth and growth-zone textures in  $\text{Toz}_{4\text{-VI}}$  and  $\text{Wf}_{1\text{-III}}$  in contact with kaolinite ( $\text{Kln}_{1\text{-VI}}$ ) (crossed polars). Abbreviations according to the IMA: cst = cassiterite, fl = fluorite, kln = kaolinite, mca = mica, qtz = quartz, toz = topaz, wf = wolframite.

Figure 5: Paragenetic sequence of the Piaotang W-Sn deposit based on observations made on samples collected at three levels (-268, -388 and -556 m) of the mine galleries (modified after Legros *et al.* (2018)). Details of the different stages and petrographic descriptions are provided in Legros *et al.* (2018). Minerals in color (wolframite, quartz, cassiterite and fluorite) were chosen for this FI study. Colors are in accordance with Figures 8 to 12.

Figure 6: Textural characterization of the minerals from the Piaotang deposit selected for FI study, according to their respective stages. Modified after Legros *et al.* (2018). (A) Wolframite-cassiterite-quartz vein from Stage I. (B) Fluorite-cassiterite-quartz vein, where fluorite is late and belongs to Stage II. (C) Whole thin-section observed in natural light. (D) Same whole thin-section as that shown in (C) observed with crossed polars. The main minerals crystallizing in Stage I ( $\text{Cst}_{1\text{-I}}$ ,  $\text{Wf}_{1\text{-I}}$ ,  $\text{Qtz}_{1\text{-I}}$  and Fe-Li-mca) show complex relationships. Abbreviations according to the IMA: cst = cassiterite, fl = fluorite, mca = mica, qtz = quartz, wf = wolframite.

Figure 7: Petrography and filling phases of FIs from the Maoping and Piaotang deposits, studied at room temperature. Zooms show representative fills for each type of FI observed in isolation, within clusters or in trails. FIs from Maoping are shown in (A) to (I). FIs from Piaotang are shown in (J) to (N). (A) Two-phase liquid ( $\text{L}_{\text{aq}}$ ) + vapor

1354 (V<sub>aq</sub>) aqueous FI found as isolated irregular inclusions and intragranular FIPs (dotted  
 1355 red lines) in Qtz<sub>2-III</sub>. (B) Intragranular FIPs (dotted red lines) of two-phase liquid  
 1356 (L<sub>aq</sub>) + vapor (V<sub>aq</sub>) aqueous FI and isolated irregular three-phase liquid H<sub>2</sub>O (L<sub>aq</sub>) +  
 1357 liquid CO<sub>2</sub> (L<sub>CO2</sub>) + vapor CO<sub>2</sub> (V<sub>CO2</sub>) aquo-carbonic FI in Qtz<sub>2-III</sub>. (C) Intragranular  
 1358 FIPs of two-phase liquid (L<sub>aq</sub>) + vapor (V<sub>aq</sub>) aqueous FI and isolated irregular one-  
 1359 phase liquid (L<sub>aq</sub>) aqueous FI in Qtz<sub>2-III</sub>. (D) Two-phase liquid (L<sub>aq</sub>) + vapor (V<sub>aq</sub>)  
 1360 aqueous FIs that occur as isolated regular inclusions parallel to growth zones and  
 1361 intragranular FIPs oblique to the growth zones in Cst<sub>1-III</sub>. (E) Two-phase liquid (L<sub>aq</sub>)  
 1362 + vapor (V<sub>aq</sub>) aqueous FI isolated irregular inclusions and intragranular FIP in Wf<sub>1-III</sub>.  
 1363 (F) Two-phase liquid (L<sub>aq</sub>) + vapor (V<sub>aq</sub>) aqueous FI as isolated negative crystal-  
 1364 shape inclusions and intragranular FIP in Qtz<sub>4-IV</sub>. (G) Two-phase liquid (L<sub>aq</sub>) + vapor  
 1365 (V<sub>aq</sub>) aqueous FI as isolated regular inclusions and intragranular FIP displayed  
 1366 parallel to the growth zone in Fl<sub>1-VI</sub>. (H) Two-phase liquid (L<sub>aq</sub>) + vapor (V<sub>aq</sub>)  
 1367 aqueous FI as isolated regular inclusions and intragranular FIP along Toz<sub>4-VI</sub> growth  
 1368 zones. (I) Two-phase liquid (L<sub>aq</sub>) + vapor (V<sub>aq</sub>) aqueous FI as isolated regular  
 1369 inclusions and intragranular FIP along Fl<sub>2-VI</sub> growth zones. (J) Two-phase liquid (L<sub>aq</sub>)  
 1370 + vapor (V<sub>aq</sub>) aqueous FI as isolated irregular inclusions and intragranular FIP in  
 1371 Qtz<sub>1-I</sub>. (K) One-phase liquid (L<sub>aq</sub>) aqueous FI isolated irregular inclusions and  
 1372 intragranular FIP in Qtz<sub>1-I</sub>. (L) Two-phase liquid (L<sub>aq</sub>) + vapor (V<sub>aq</sub>) aqueous FI as  
 1373 isolated regular inclusions observed along the Wf<sub>1-I</sub> c-axis and in secondary FIP  
 1374 crossing the Wf<sub>1-I</sub> c-axis. (M) Two-phase liquid (L<sub>aq</sub>) + vapor (V<sub>aq</sub>) aqueous FI as  
 1375 isolated regular inclusions displayed along a Cst<sub>1-I</sub> growth zones and secondary FIP  
 1376 crossing the Cst<sub>1-I</sub> growth zones. (N) Two-phase liquid (L<sub>aq</sub>) + vapor (V<sub>aq</sub>) aqueous  
 1377 FI as isolated regular inclusions and intragranular FIP in Fl<sub>1-II</sub>. Abbreviations

according to the IMA: cst = cassiterite, fl = fluorite, qtz = quartz, toz = topaz, wf = wolframite.

Figure 8: Microthermometric and Raman spectroscopy data on two-phase aqueous FIs for the Maoping and Piaotang deposits. (A) Binary salinity vs.  $T_h$  diagram for Maoping FIs at all stages in quartz, cassiterite and wolframite from the W-Sn mineralized stage III, quartz crystallized in the banded quartz veins on stage IV and fluorite and topaz in late stage VI. (B) Binary salinity vs.  $T_h$  diagram for Piaotang FIs at all stages in quartz, cassiterite and wolframite from the silicate-oxide mineralizing stage I and late fluorite from the carbonate stage II. For both Maoping and Piaotang data, possible fluid end-members are indicated by letters from (A) to (D). Serrated sides of the boxes indicate the direction along which the exact position of the actual end-member should be. (C) Gas concentrations obtained by Raman spectroscopy on the vapor phase of FIs hosted in Qtz<sub>2-III</sub> and Cst<sub>1-III</sub> at Maoping and Cst<sub>1-I</sub> from stage I at Piaotang are represented in a ternary diagram showing relative molar proportions of CO<sub>2</sub>, CH<sub>4</sub> and N<sub>2</sub>.

Figure 9: Minimum and maximum trapping condition isochores drawn for all end-members determined from two-phase aqueous FIs from the Maoping (A) and Piaotang (B) deposits. Estimation of the PT conditions of fluid trapping requires intersecting the FI isochores by independent P or T constraints. The wet-saturated solidus of granitic magmas (Joyce and Voigt, 1994) defines the maximum PT conditions of the investigated fluids. To draw the geothermal gradients in the PT diagram, pressure conditions must be assumed to be either lithostatic or hydrostatic. The Maoping and Piaotang systems are interpreted to have formed under hydrostatic conditions

because both deposits were formed during multiple fluid pulses that were not in equilibrium with the surrounding rocks. Geothermal gradients with values between 30°C/km (normal crustal gradient) and 90°C/km (gradients typical of high temperature geothermal systems) have been drawn. The minimum and maximum pressures are also constrained by the range of common emplacement depths for the granitic pluton (5-10 km; e.g. Audétat *et al.*, 2000; Chicharro *et al.*, 2016).

Figure 10: Major and trace element concentrations in FIs from the Maoping and Piaotang deposits, as determined by LA-ICPMS analysis. All concentrations are expressed in ppm. (A) Qtz<sub>2-III</sub>, (B) Cst<sub>1-III</sub>, (C) Qtz<sub>4-IV</sub>, (D) Fl<sub>1-VI</sub> and (E) Toz<sub>4-VI</sub> from the Maoping deposit. (F) Qtz<sub>1-I</sub>, (G) Cst<sub>1-I</sub> and (H) Fl<sub>1-II</sub> from the Piaotang deposit. Each symbol represents a single ablated fluid inclusion. Full symbols represent calculated values that are above the LODs. Empty symbols represent the LODs when an element was considered undetected.

Figure 11: Selected element concentration relationships from LA-ICPMS analyses of fluid inclusions from the Maoping and Piaotang deposits. Each symbol represents a single ablated fluid inclusion. (A) Na-K-Li(x10) ternary diagram. The compositions are calculated as a function of their respective concentrations expressed in ppm. Lines indicating equal values for K:Na and Li:Na molar ratios (1:1 and 1:10) are in grey. (B) and (C) Na vs. Li and Na vs. K binary concentration diagrams. Lines indicate equal values for K:Na and Li:Na molar ratios (1:1 and 1:10) in grey. (D) K/Rb vs. Cs concentration diagram where K/Rb is expressed as a function of the respective concentrations expressed in ppm. Boxes representing the possible fluid reservoirs are

shown in each binary diagram. The exact position of these reservoirs on the respective diagrams are not known and are therefore indicated by dashed lines.

Figure 12: Stable isotope (O, H) data for minerals and fluids from the Maoping and Piaotang deposits. (A) Oxygen isotopic compositions of minerals (empty symbols) and calculated equilibrium compositions for fluids according to temperature estimates from FI isochores. (B) Hydrogen isotopic compositions of FIs. (C) Extracted temperature estimates from isochores. Fe-Li-micas are interpreted as co-precipitating with Qtz<sub>2-III</sub> and Cst<sub>1-III</sub> at the Maoping deposit. (D) Binary  $\delta D$  vs.  $\delta^{18}O$  diagram for the fluids from the Maoping and Piaotang deposits. Compositions of metamorphic waters and felsic magmatic waters are after Sheppard (1994). Boxes for the possible fluid reservoirs are shown. The exact positions of these reservoirs on the respective diagrams are not known and are therefore indicated by dashed lines. The box on the meteoric water line represents possible local meteoric water in accordance with Wei *et al.* (2012). Grey dashed lines indicate possible mixing trends between magmatic fluids and meteoric waters. The arrow illustrates the possible evolution of the magmatic fluid end-member associated to degassing according to Hedenquist and Lowenstern (1994). Grey transparent boxes in the background represent isotopic data from Chinese W-Sn deposits (dark grey with dashed edges) and worldwide deposits as synthesized/compiled in Marignac and Cathelineau, 2009 (light grey).

Figure 13: Compilation of fluid inclusion microthermometric data from the literature. Each data point represents one deposit. The compiled data show the  $T_h$  and salinity measured for fluids interpreted to be involved in ore-forming processes only. For homogeneity, ranges represent the minimum and maximum values acquired by the



1452 author. For better readability, (A) shows data from deposits worldwide and (B)  
 1453 shows data measured for W-Sn deposits from the South China Craton only. Deposits  
 1454 are referred to in the figure as: [1] Brandberg, Namibia, [2] Karagwe-Ankole,  
 1455 Rwanda, [3] Kibaran, Rwanda, [4] Nyakabingo, Rwanda, [5] Grey River, Canada,  
 1456 [6] Mount Pleasant, Canada, [7] New ross area, Canada, [8] Tombstone belt, Canada,  
 1457 [9] Sweet home mine, USA, [10] Correias, Brazil, [11] Julcanie, Peru, [12] Pasto  
 1458 Buena, Peru, [13] San Cristobal, Peru, [14] Bankura, India, [15] Degana, India, [16]  
 1459 Ohtani and Kaneuchi, Japan, [17] Hwanggangri, Korea, [18] Kyzylto, Mongolia,  
 1460 [19] Triginoe, Russia, [20] Hub stock, Czech Republic, [21] Carrock fell, England,  
 1461 [22] Cligga Head, England, [23] Beauvoir, France, [24] Ehrenfriedersdorf, Germany,  
 1462 [25] Zinnwald, Germany, [26] Carris, Portugal, [27] Panasqueira, Portugal, [28]  
 1463 Logrosan, Spain, [29] Spanish central system, [30] Aberfoyle, Australia, [31]  
 1464 Herberton, Australia, [32] Mole granite, Australia, [33] Dajishan, China, [34]  
 1465 Dangping, China, [35] [36] Maoping, China, [37] Pangushan, China, [38] [39]  
 1466 Piaotang, China, [40] Shimenshi, China, [41] Taoxikeng, China, [42] Xihuashan,  
 1467 China, [43] Shizuyuan, China, [44] Yaogangxian, China, [45] Yejiwei, China.  
 1468 Associated references, host mineral and gas contents are listed in the table in  
 1469 Appendix A. Critical and halite saturation curves are from Wilkinson (2001).  
 1470 Possible fluid end-members interpreted from our study of the Maoping and Piaotang  
 1471 deposits are indicated by letters (A) to (D). Serrated sides of the boxes indicate the  
 1472 direction along which the exact position of the actual end-member should be.

1473     **Table 1 – Petrography, Raman spectroscopy and microthermometry data for fluid inclusions from the Maoping and Piaotang deposits. Values in parentheses indicate modes.**

Mineral	Phases at 25 °C	Proportion within a crystal (visual estimation)	Petrography	Morphology	Size / μm	α (%) (25°C)	N	Microthermometry				Salinity
	(trace gases after Raman spectroscopy)							T <sub>m</sub> (ice)	T <sub>m</sub> (cla)	T <sub>h</sub> (CO <sub>2</sub> ) (to vapor)	T <sub>h</sub> (to liquid)	/ wt. % equiv. NaCl
MAOPING												
Stage III: W-Sn veins												
Quartz <sub>2-III</sub>	L <sub>aq</sub> -V <sub>aq</sub> + trace CO <sub>2</sub> >CH <sub>4</sub> >N <sub>2</sub>	85%	intragranular FIP or isolated	irregular	5-30	20-50	96	-4.5 to -0.2 (-0.7)	-	-	157 to 287 (220)	0.4 to 9.0 (1.3)
	L <sub>aq</sub> -L <sub>CO<sub>2</sub></sub> -V <sub>CO<sub>2</sub></sub>	5%	isolated or cluster	irregular	10-20	85-95	6	-1.7 to -0.9 (-1.2)	7.7 to 8.1 (8.0)	29.4 to 30.6 (30.3)	200 to 252 (230)	0.4 to 0.5 (0.4)
	L <sub>aq</sub>	10%	intragranular FIP or isolated	irregular	5-30	20-50	°	-	-	-	-	-
Wolframite <sub>1-III</sub>	L <sub>aq</sub> -V <sub>aq</sub> <sup>a</sup>	100%	FIP along growth zone or intragranular	regular	5-25	20-50	30	-5.2 to -3.7 (-4.4)	-	-	284 to 346 (340)	7.2 to 10.5 (8.7)
Cassiterite <sub>1-III</sub>	L <sub>aq</sub> -V <sub>aq</sub> + trace CO <sub>2</sub> >CH <sub>4</sub> >N <sub>2</sub>	100%	FIP along growth zone or isolated	irregular	10-20	30-60	25	-5.5 to -3.0 (-3.8)	-	-	299 to 338 (340)	5.8 to 11.2 (7.5)
Stage IV: Banded quartz veins												
Quartz <sub>4-IV</sub>	L <sub>aq</sub> -V <sub>aq</sub> + trace CO <sub>2</sub>	100%	intragranular FIP	regular	5-15	20-30	41	-6.1 to -1.3 (-4.2)	-	-	148 to 291 (240)	7.7 to 12.6 (9.0)
Stage VI: Late phases												
Fluorite <sub>1-VI</sub>	L <sub>aq</sub> -V <sub>aq</sub> <sup>b</sup>	100%	FIP along growth zone or intragranular	regular	5-15	30-60	20	-5.4 to -4.3 (-4.5)	-	-	195 to 325 (340)	8.1 to 11.1 (9.0)
Topaz <sub>4-VI</sub>	L <sub>aq</sub> -V <sub>aq</sub> + trace CO <sub>2</sub>	100%	FIP along growth zone or clusters	irregular	5-30	10-50	46	-4.2 to -3.3 (-3.9)	-	-	307 to 346 (340)	5.6 to 7.0 (6.1)
Fluorite <sub>2-VI</sub>	L <sub>aq</sub> -V <sub>aq</sub> <sup>b</sup>	100%	FIP along growth zone	regular	5-20	10-20	15	-0.9 to -0.1 (-0.1)	-	-	136 to 292 (230)	0 to 1.6 (0.1)
PIAOTANG												
Stage I: Silicate-oxide												
Quartz <sub>1-I</sub>	L <sub>aq</sub> -V <sub>aq</sub>	100%	intragranular FIP or isolated	irregular	5-15	10-30	20	-2.2 to -0.2 (-2.2)	-	-	144 to 175 (160)	0.4 to 3.8 (2.2)
	L <sub>aq</sub>	10%	intragranular FIP or isolated	irregular	5-15	10-30	°	-	-	-	-	-
Wolframite <sub>1-I</sub>	L <sub>aq</sub> -V <sub>aq</sub> <sup>a</sup>	100%	FIP along growth zone	regular	5-15	10-40	18	-5.3 to -3.1 (-4.2)	-	-	173 to 222 (210)	5.6 to 8.3 (6.5)
Cassiterite <sub>1-I</sub>	L <sub>aq</sub> -V <sub>aq</sub> + trace CO <sub>2</sub> >CH <sub>4</sub> >N <sub>2</sub>	100%	FIP along growth zone or intragranular	regular	5-20	10-40	24	-3.7 to -1.4 (-3.5)	-	-	283 to 349 (340)	2.4 to 6.2 (5.8)
Stage II: Calcic stage												
Fluorite <sub>1-II</sub>	L <sub>aq</sub> -V <sub>aq</sub> <sup>b</sup>	100%	intragranular FIP or isolated	regular	15-40	10-30	23	-5.0 to 0.0 (0)	-	-	142 to 185 (170)	0 to 7.7

<sup>a</sup> **Wolframite is an opaque mineral and could not therefore be analyzed by Raman spectroscopy**

<sup>b</sup> **Due to fluorescence, it was impossible to observe gas peaks by Raman spectroscopy**

<sup>c</sup> **Phase transitions could not be observed in one-phase liquid inclusions**

**Abbreviations: α = vapor phase, L = liquid, V = vapor, aq = aqueous, FIP = fluid inclusion plane, T<sub>m</sub> = melting temperature, T<sub>h</sub> = homogenization temperature, cla = clathrate**

1475      **Table 2 - LA-ICPMS measurements made on fluid inclusions from the Maoping and Piaotang deposits. Values preceded by a < symbol stand for element concentrations below the limit of detection. N.A. = not analyzed**

MAOPING	Salinity / wt.% equiv. NaCl	Li / ppm	Na / ppm	Mg / ppm	K / ppm	Ca / ppm	Mn / ppm	Rb / ppm	Sr / ppm	Y / ppm	Nb / ppm	Mo / ppm	Sn / ppm	Cs / ppm	Ba / ppm	Ta / ppm	W / ppm	Na/Li (molar ratio)	Na/K (molar ratio)	Na/Ca (molar ratio)	K/Rb (mass ratio)
Quartz <sub>2-III</sub>	1.3	37	1000	43	490	<5200	160	2	<1.5	<1.6	<1.4	<8.6	42	<1	<1.4	<1.1	24	8.4	3.3	-	196
	1.5	84	1600	28	530	<4000	810	7	<1.5	<1.1	<1.4	58	18	1.8	3.0	<1	41	5.8	5.0	-	75
	0.5	41	1200	55	110	<410	74	<1	<1	<1	<1	11	4.7	2.8	8.5	<0.06	7.8	9.1	10.0	-	-
	6	360	13000	220	9000	<24000	180	22	11	<7.6	<8.5	<37	49	18	<9.2	<3.9	<21	11.3	2.5	-	414
	1.5	61	2300	32	500	2500	120	<1	1.0	<1	<1	4.4	37	6.0	1.3	<1	10	11.7	10.0	1.7	-
Cassiterite <sub>1-III</sub>	4.1	250	6300	180	1200	<21300	220	<11	<8.3	<7.9	<6.6	<39	73	26	<7.9	<3.7	<18	7.7	10.0	-	-
	8.3	2600	17000	<60	9500	<25000	1280	660	<8	<11	<65	<55	N.A.	960	<8	<61	<40	2.0	3.3	-	14
	10	3200	26000	<50	4300	<21000	<90	650	<10	<5	<40	<35	N.A.	500	<7	<31	<34	2.4	10.0	-	7
	8.5	2300	19000	<250	8500	<96000	<420	540	<38	<20	<230	<170	N.A.	700	<21	<170	150	2.6	3.3	-	16
	8.5	1800	20000	<430	10000	<138000	1000	560	<47	<44	<200	<250	N.A.	640	<55	<190	<170	3.3	3.3	-	18
	8.5	3200	20000	<54	2400	<25000	<110	280	<7	<9	33	<45	N.A.	410	<8	<22	<28	1.9	10.0	-	9
Quartz <sub>4-IV</sub>	8.5	1600	21000	<250	10400	<91000	970	390	<31	<34	<460	<110	N.A.	460	<27	<840	<80	4.0	3.3	-	27
	9	2200	18500	<150	8700	<43000	4200	320	<16	<12	<14	110	450	60	16	<13	270	2.5	3.3	-	27
	9	<90	6000	<51	9800	20000	450	250	<6	<5	<5	57	<67	9	<4	5	160	-	1.0	0.6	39
	9	90	1400	8300	1600	<17000	500	<9	9	<5	<6	<48	140	<4	<5	<3	220	4.9	1.4	-	-
	9	260	7000	9900	2200	<12000	1400	27	10	<4	<3	83	120	40	<4	<2	300	8.1	5.0	-	82
Fluorite <sub>1-VI</sub>	9	400	7300	5300	4800	<19000	760	19	7	<5	<6	87	220	23	6	<4	200	5.5	2.5	-	250
	8	<2200	27700	<970	<15600	N.A.	<1800	<240	1100	<2400	<130	<780	<1800	<120	<140	<75	<340	-	-	-	-
	9	<2800	34100	<1200	<19200	N.A.	<2500	<290	370	<4800	<200	<870	2800	<140	<200	<79	<430	-	-	-	-
	9.6	<890	37700	<450	<6250	N.A.	<830	<120	<82	<1700	<59	<220	<710	220	<73	<21	<150	-	-	-	-
Topaz <sub>4-VI</sub>	1	<55	3900	<26	<400	N.A.	<49	<5	<4	<85	<4	<20	<45	<3	<4	<2	<9	-	-	-	-
	6.4	230	20000	<13	<1700	<7600	79	330	<3	<2	<2	<27	200	310	<2	1	190	27.5	-	-	-
	6.4	1600	19000	<38	<18000	<23000	360	560	12	<6	<6	<100	100	660	<5	<4	<56	3.8	-	-	-
	6.4	280	3200	<1	36000	<1100	120	170	<1	1	<1	<4	7	150	<1	<1	10	3.5	0.1	-	1200
	6.4	280	6400	<7	27000	<4700	99	730	2	2	<2	<12	54	340	<1	<1	190	6.9	0.4	-	200
	6.4	1500	9400	5	12000	<3500	65	630	2	<1	<1	<8	18	420	<1	1	160	2.0	1.2	-	37
	6.4	710	10000	120	13000	<6400	380	730	4	430	5	<13	140	910	<2	5	180	4.4	1.4	-	19
	6.4	1400	6500	33	8200	<11000	580	910	<8	<28	7	<36	<66	850	<15	7	420	4.8	0.8	-	9
	6.4	1000	10000	<44	18000	<13000	440	1400	<9	<11	<10	<48	150	1000	<25	<14	240	9.3	0.5	-	13
	6.4	1200	14000	<33	10000	<8600	300	1000	62	<3	<6	<23	110	1500	<24	<6	190	11.4	1.4	-	10
PIAOTANG	6.4	980	10000	<33	13000	<12000	660	1600	<9	34	<5	<25	<71	2300	<16	<4	160	10.2	0.8	-	8
	4.9	200	2300	670	<350	13000	<38	<3	<3	<3	<2	<20	100	4	30	<2	<7	10.7	-	0.3	-
	4.7	98	5400	120	670	10000	<18	7	19	<1	<2	10	200	18	6	<1	<4	54.6	10.0	0.9	99
	4.5	<31	4100	35	1500	10000	<29	8	<3	<2	<2	<10	<22	4	19	<1	5	-	2.0	0.7	190
	4.7	400	9100	<37	2200	<14000	1000	49	<6	<4	<4	<20	<41	5	<5	<3	<10	22.8	5.0	-	45
	3.1	120	3400	100	160	6400	30	<3	<2	<1	<1	12	130	4	43	9	<850	28.5	0.0	1.0	-
	3.7	80	1530	560	1200	9200	71	9	3	<2	<2	17	330	11	<5	<1	<350	19.0	1.2	0.3	130
	5.2	180	16338	15	1200	<2800	330	150	2	<2	<1	<8	62	<400	<5	<1	<5	89.2	10.0	-	8
	0.9	10	960	430	450	1200	9	2	3	<1	<1	<1	51	1	1	<1	<1	98.4	2.0	1.4	200
	7.9	2400	17000	<59	7400	<21000	<94	350	<8	<6	10	<40	N.A.	600	<6	<3	130	2.1	3.3	-	21
	8.3	2400	18000	<52	5700	<14000	<63	200	<5	<5	<5	<29	N.A.	430	<6	<2	<18	2.3	5.0	-	27
	9.6	2800	23000	<21	7400	<8500	<37	350	<3	<3	25	<14	N.A.	750	<2	<2	<9	2.5	5.0	-	21
	9.6	2300	23000	<80	11400	<27000	<123	420	<9	<9	<23	<49	N.A.	560	<7	<5	<37	3.1	3.3	-	27
	7.6	2400	17000	<44	8200	<16000	<72	350	<5	<6	15	<36	N.A.	800	<6	7	<22	2.2	3.3	-	23
	8	2900	18000	<50	4400	<17000	<80	220	<7	<7	71	<36	N.A.	610	<6	14	<23	1.8	10.0	-	20
	10.3	3700	23000	<12	8700	<4300	<20	240	<1	<1	<2	<7	N.A.	780	<1	1	9	1.9	5.0	-	36
	6.2	1800	13000	<41	4600	<20000	110	160	<8	<6	41	<23	N.A.	400	<8	<3	130	2.2	5.0	-	28
	9.6	3300	22000	<56	7500	<31000	<140	220	<11	<12	<14	<51	N.A.	490	<11	<6	220	2.1	5.0	-	34
	6.2	1800	15000	<90	4500	<32000	<150	200	<11	<10	<12	<63	N.A.	460	<12	<5	<40	2.6	5.0	-	23
	7.4	2200	16000	<29	7500	<12000	280	250	<5	<4	15	<24	N.A.	600	<4	<2	140	2.2	3.3	-	30
	9.6	290	18000	300	1700	N.A.	120	39	3200	27	<1	<6	340	61	15	2	16	18.5	10.0	-	44
	9.6	510	32000	690	3700	N.A.	280	93	<220	<5	<3	32	360	150	14	3	<7	19.0	10.0	-	40
	4.7	310	11000	40	1100	N.A.	<8	31	1100	20	<1	<4	12	32	2	1	<1	10.5	10.0	-	36
	4.7	21	1100	40	<78	N.A.	38	3	3300	10	<1	9	74	7	<1	1	10	15.7	-	-	-
	9.6	650	29000	390	2400	N.A.	250	100	770	<15	<15	<88	390	120	<47	<8	<42	44.2	10.0	-	30
	4.7	260	12000	1200	5200	N.A.	<320	<69	<540	<48	<35	<200	<360	70	<95	<22	<110	45.9	2.5	-	25
	9.6	300	13000	1500	1500	N.A.	110	110	3700	71	<4	<22	59	41	<15	<3	<14	44.8	10.0	-	-
	9.6	110	26000	800	1300	N.A.	63	50	1700	100	<3	<16	60	33	23	<1	<9	226.0	-	-	14
	9.6	530	24000	470	5600	N.A.	<100	130	1400	28	<10	<58	530	160	<32	<6	<33	45.7	5.0	-	26
	10	670	31000	200	2900	N.A.	62	96	720	<1	<1	<4	<8	140	2	1	<1	14.1	10.0	-	43

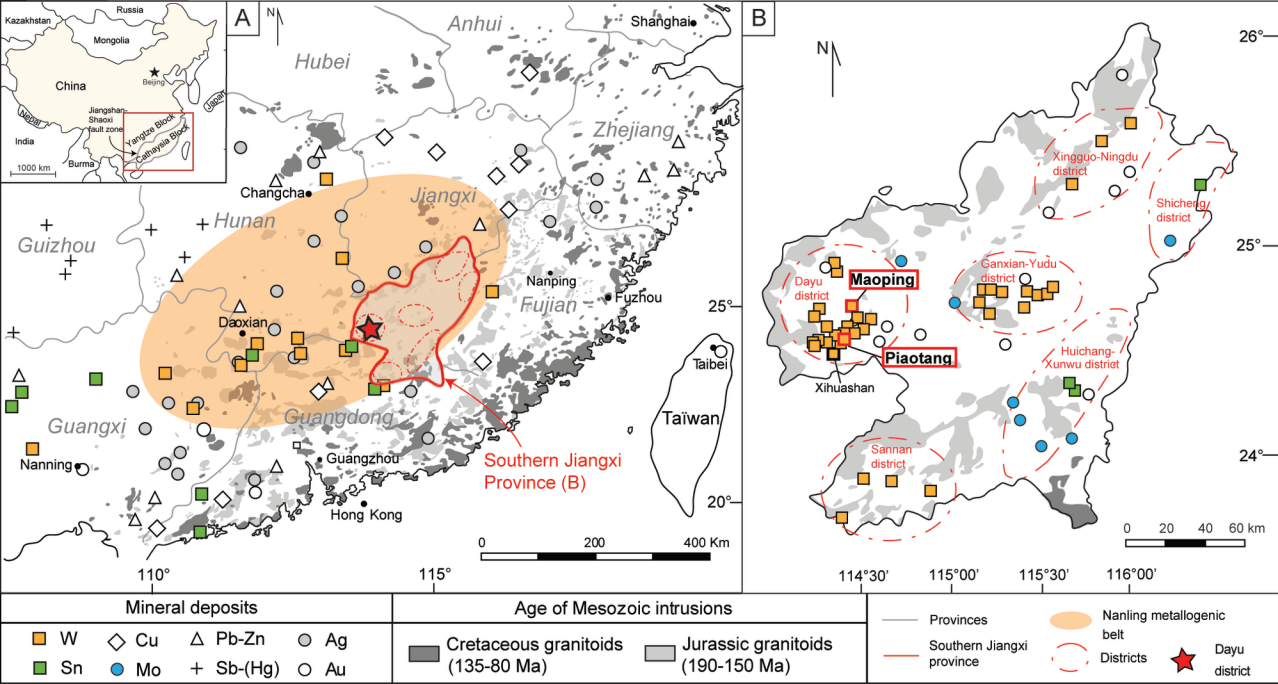
1477     **Table 3 – Stable isotope (O, H) results for minerals and fluids from the Maoping and Piaotang deposits.**

Mineral	$\delta^{18}\text{O}$ / ‰VSMOW <sub>mineral</sub> measured	T range / °C estimated from isochores	$\delta^{18}\text{O}$ / ‰VSMOW <sub>fluid</sub> calculated	$\delta\text{D}$ / ‰VSMOW <sub>fluid</sub> measured
<b>MAOPING</b>				(min. to max.)
<i>Stage II: Fe-Li-mica veins</i>				
Fe-Li-micas <sub>2-II</sub>	8.3	180-340	2.8 to 7.5	-
<i>Stage III: W-Sn veins</i>				
Quartz <sub>2-III</sub>	10.9	180-340	-2.1 to 5.1	-59 to -55 (N=3)
Wolframite <sub>1-III</sub>	0.5	350-440	2.8 to 3.4	-78 to -77 (N=3)
Cassiterite <sub>1-III</sub>	-	360-450	-	-72 (N=1)
Fe-Li-micas <sub>3-III</sub>	8.7	360-450	8.2 to 9.1	-
<i>Stage IV: Banded quartz veins</i>				
Quartz <sub>4-IV</sub>	10.8	180-380	-2.2 to 5.9	-66 to -62 (N=2)
<i>Stage VI: Late phases</i>				
Topaz <sub>4-VI</sub>	8.4	380-440	7.4 to 8.1	-
<b>PIAOTANG</b>				
<i>Stage I: Silicate-oxide</i>				
Quartz <sub>1-I</sub>	11.6	170-240	-2.2 to 2.2	-54 to -51 (N=2)
Wolframite <sub>1-I</sub>	-3.0	200-290	-3.6 to -2.4	-77 to -76 (N=2)
Cassiterite <sub>1-I</sub>	-	360-460	-	-70 to -58 (N=3)

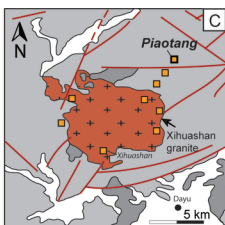
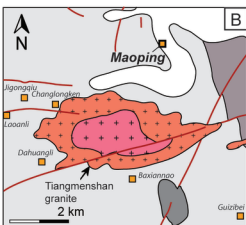
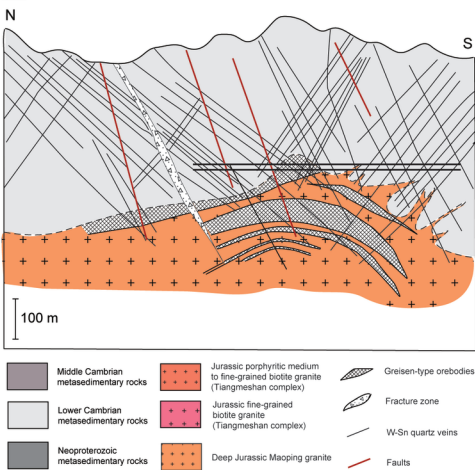
1478

Country	Name	Host mineral	Salinity	Th	Content					Reference	
					Aqueous	CO2	CH4	N2	Halite cube		on Fig. 13
<b>Africa</b>											
Namibia	Brandberg	quartz	1.8-11.7	152-224	x	x			x	Macey and Harris, 2006	1
	Karagwe-Ankole	tourmaline	7.7-21.4	269-398	x	x				Hulsbosch <i>et al.</i> , 2016	2
Rwanda	Kibaran	quartz	13-17	130-300	x	x				Pohl and Günther, 1991	3
	Nyakabingo	wolframite	3.2-4.5	240-320	x	x				Dewaele <i>et al.</i> , 2016	4
<b>America (North)</b>											
Canada	Grey River	scheelite	1.9-5.1	265-285	x					Higgins, 1985	5
	Mount Pleasant	quartz	10-42	260-490	x				x	Davis and Williams-Jones, 1985	6
	New Ross area	quartz	0-43	80-370	x				x	Carruzzo <i>et al.</i> , 2000	7
	Tombstone belt	quartz	0.2-8	174-355		x	x		x	Baker and Lang, 2001	8
USA	Sweet Home mine	wolframite	5.7-6.3	325-355	x					Lüders <i>et al.</i> , 2009	9
<b>America (South)</b>											
Brazil	Correas	quartz	1-18	340-440	x	x	x			Bettencourt <i>et al.</i> , 2005	10
	Julcanie	wolframite	10.9-17.2	287-322	x					Deen <i>et al.</i> , 1994	11
Peru	Pasto Buena	various	2-17	175-290	x	x			x	Landis and Rye, 1974	12
	San Cristobal	quartz	2.1-5.1	146-257	x	x			x	Beuchat <i>et al.</i> , 2004	13
<b>Asia</b>											
India	Bankura	quartz	8-17	230-370	x	x			x	Mishra <i>et al.</i> , 1999	14
	Degana	quartz	8-33	118-425		x			x	Krylova <i>et al.</i> , 2012	15
Japan	Ohtani and Kaneuchi	quartz	3.7-8.2	190-530		x	x		x	Morishita <i>et al.</i> , 1991	16
Korea	Hwanggangri	various	0.5-10	285-370	x	x				So and Yun, 1994	17
Mongolia	Kyzyltau	various	2-32	113-432	x	x	x	x	x	Graupner <i>et al.</i> , 1999	18
Russia	Tigrinoe	quartz	3-7	240-420	x					Krylova <i>et al.</i> , 2012	19
<b>Europe</b>											
Czech Republic	Hub stock	various	0.6-3.2	330-470		x	x	x		Dolnicek <i>et al.</i> , 2012	20
England	Carrock Fell	various	6	235-335	x	x				Ball <i>et al.</i> , 1985	21

France	Cligga Head	cassiterite	6.5-7.9	290-370	x					Smith <i>et al.</i> , 1996	22
	Beauvoir	quartz	1.4-48.2	305-600	x	x	x	x		Harlaux <i>et al.</i> , 2017	23
	Ehrenfriedersdorf	quartz	5-50	380-480	x					Rickers <i>et al.</i> , 2006	24
Germany	Zinnwald	wolframite	10-12	340-350	x					Korges <i>et al.</i> , 2017	25
Portugal	Carris	scheelite	3-8	230-280	x	x		x	x	Moura <i>et al.</i> , 2014	26
	Panasqueira	quartz	5-10	230-360	x		x		x	Polya <i>et al.</i> , 2000	27
Spain	Logrosan	various	0.4-11	280-400		x	x	x		Chicharro <i>et al.</i> , 2016	28
	Spanish central system	quartz	0.2-1.8	310-340		x	x			Vindel <i>et al.</i> , 1995	29
<b>Oceania</b>											
Australia	Aberfoyle	various	6-45	175-400	x	x			x	Hoffman <i>et al.</i> , 1988	30
	Herberton	various	0-50	13-460	x	x			x	Charoy and Polard, 1989	31
	Mole granite	quartz	2.1-40.7	350-563	x				x	Audétat <i>et al.</i> , 2000	32
<b>South China Block</b>											
Jiangxi, China	Dajishan	wolframite	4.3-9	240-370	x					Ni <i>et al.</i> , 2015	33
	Dangping	wolframite	6.7-8.7	284-324	x					Ni <i>et al.</i> , 2015	34
	Maoping	wolframite	4.6-8.8	292-362	x	x				Chen <i>et al.</i> , 2018	35
		wolframite	5.8-11.2	284-346	x					This study	36
	Pangushan	quartz	3.1-8	240-366	x					Ni <i>et al.</i> , 2015	37
		wolframite	4.6-8.9	280-390	x					Ni <i>et al.</i> , 2015	38
	Piaotang	wolframite	5.6-8.3	173-222						This study	39
		quartz	0.5-9.5	162-363	x	x	x	x		Gong <i>et al.</i> , 2015 (in chinese)	40
	Taoxikeng	quartz	8	310-390						Wang <i>et al.</i> , 2012	41
	Xihuashan	wolframite	3.8-13.7	239-380	x					Wei <i>et al.</i> , 2012	42
	Shizhuyuan	quartz	-	230-300						Xuexin <i>et al.</i> , 1990	43
	Yaogangxian	quartz	4.5-15.2	212-386						Hu <i>et al.</i> , 2012	44
Hunan, China	Yejiwei	quartz	-	220-240						Xuexin <i>et al.</i> , 1990	45

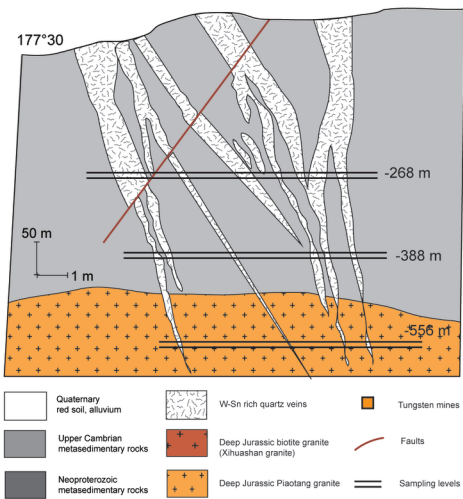


# A MAOPING DEPOSIT

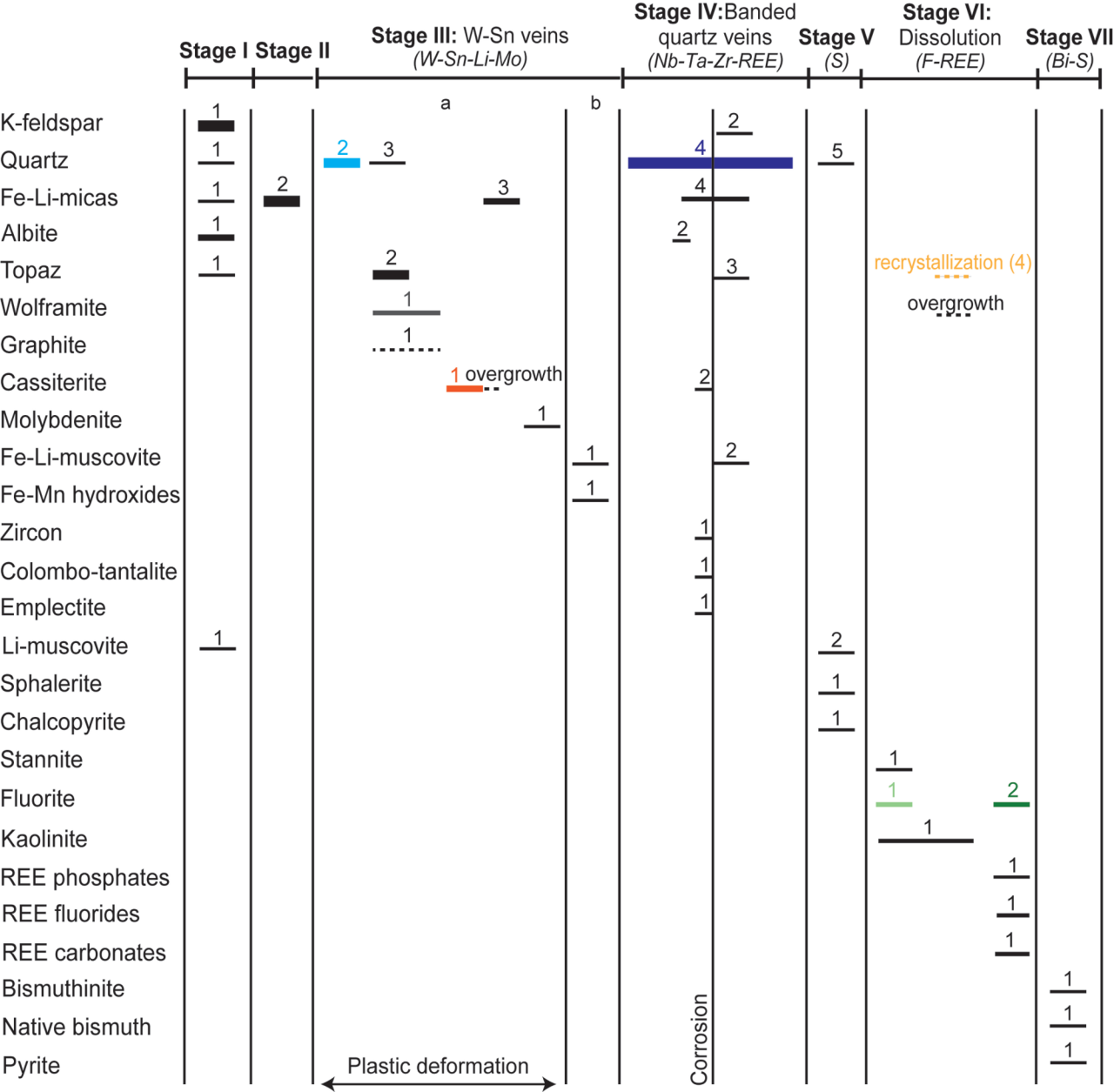


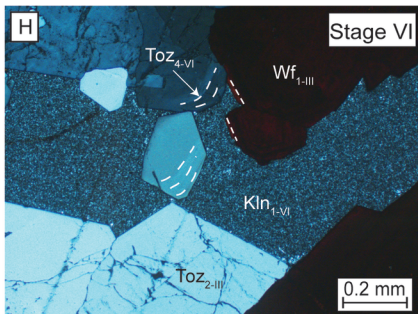
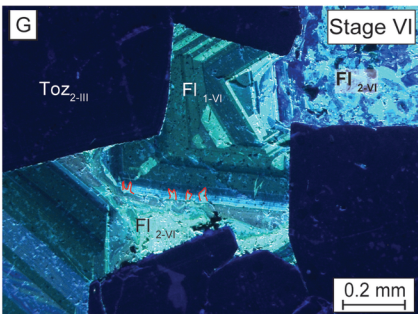
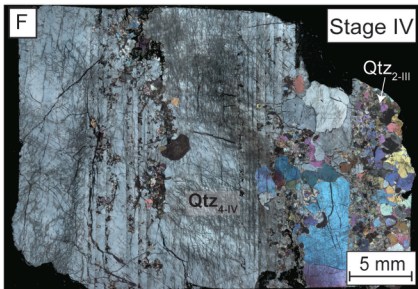
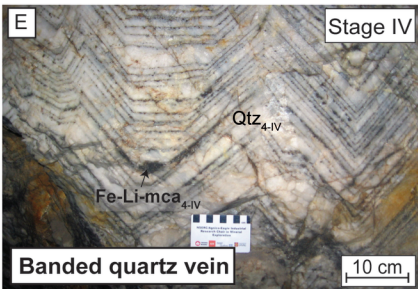
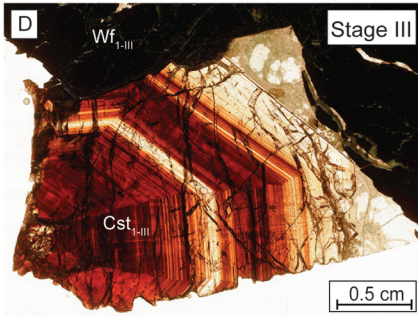
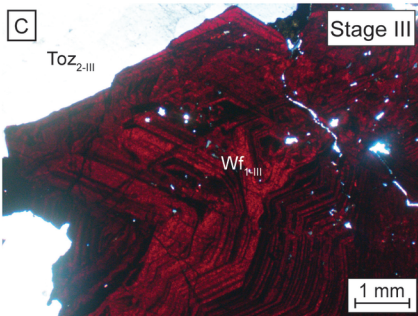
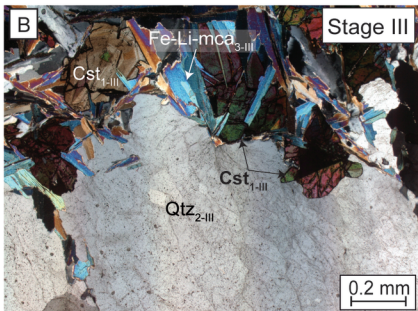
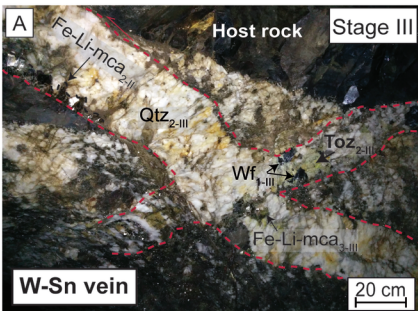
# D PIAOTANG DEPOSIT

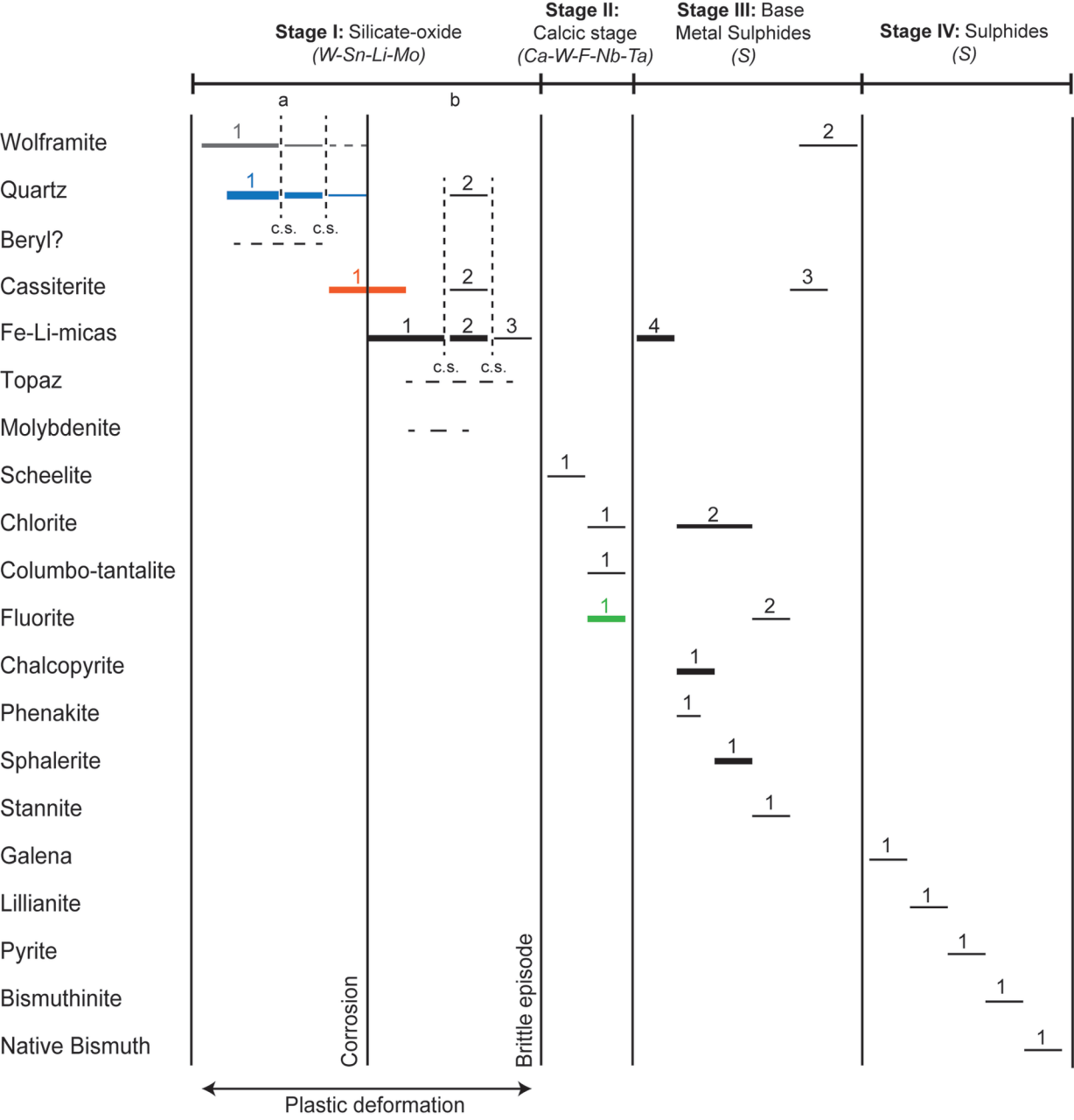
357°30



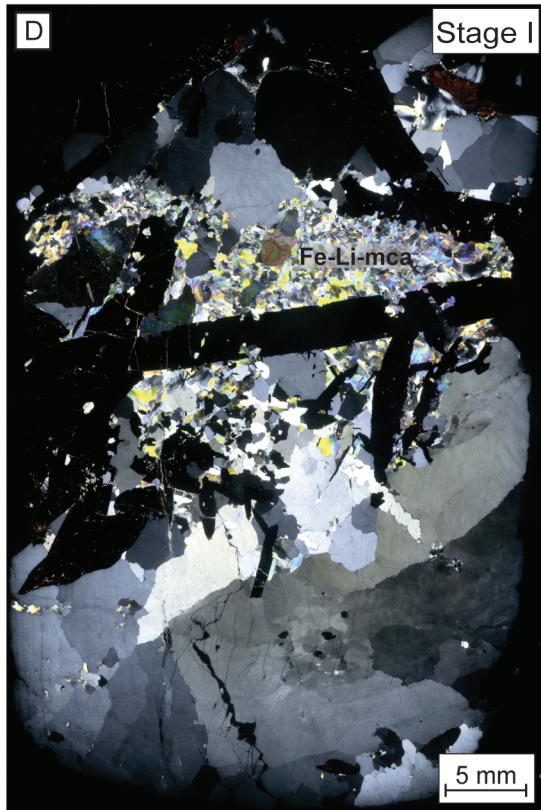
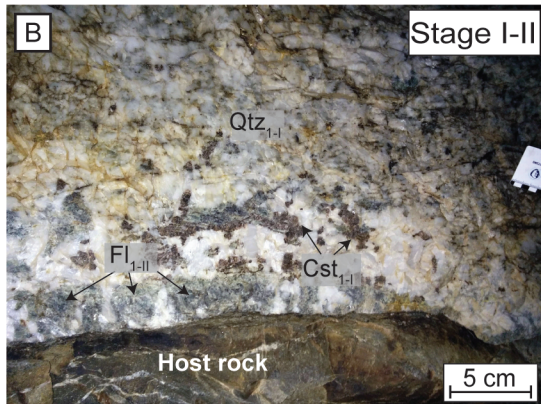
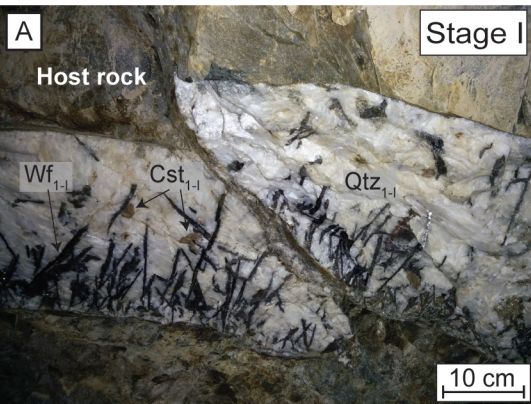


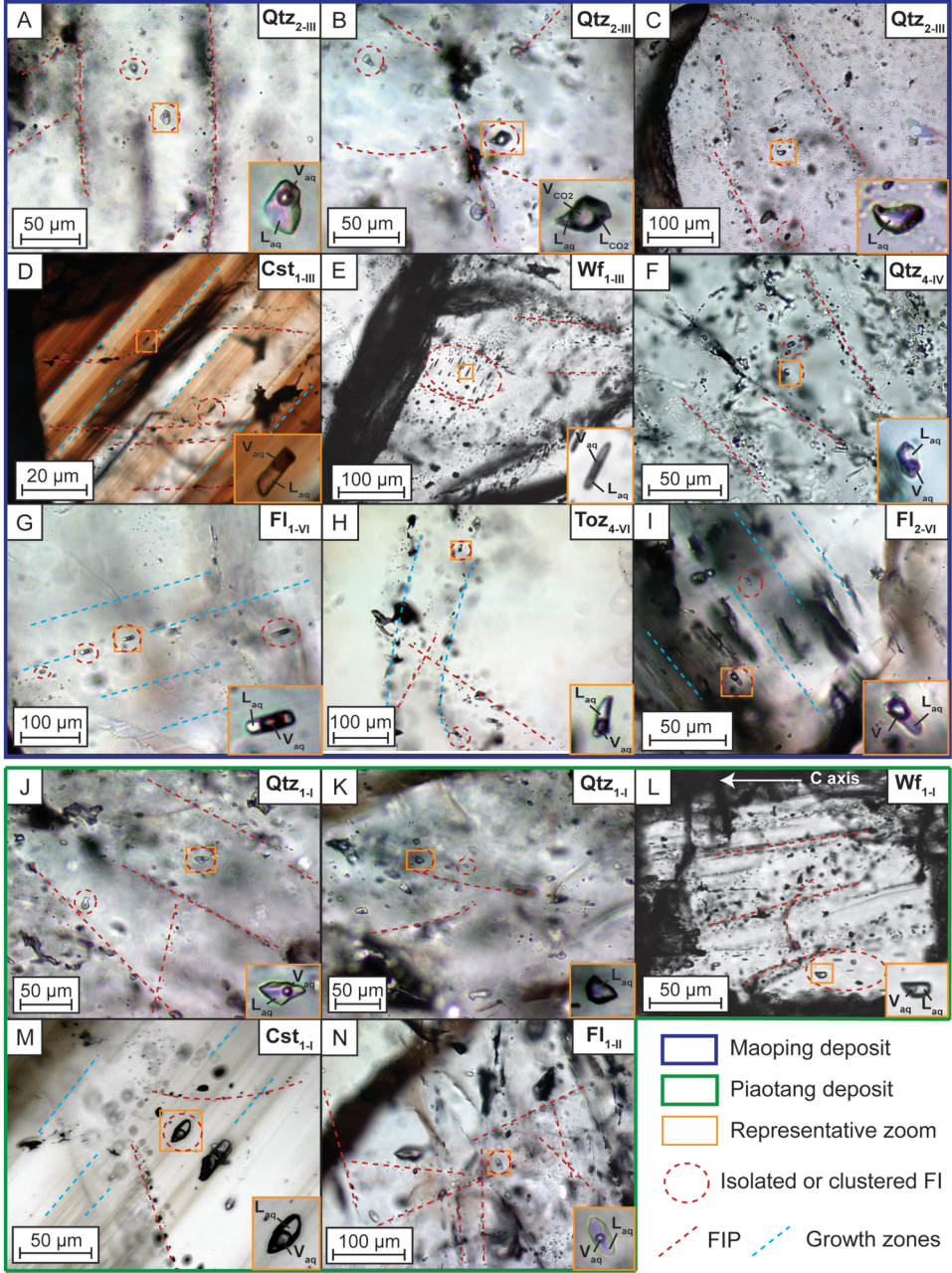




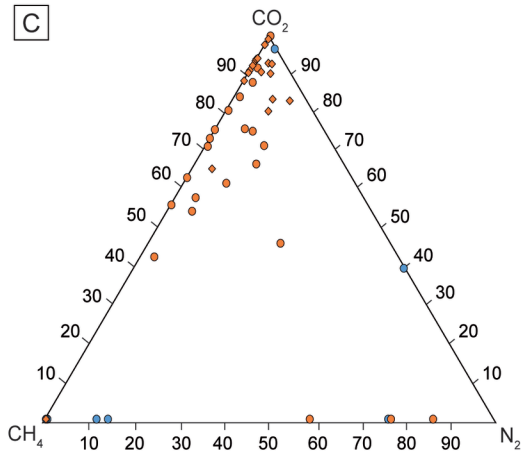
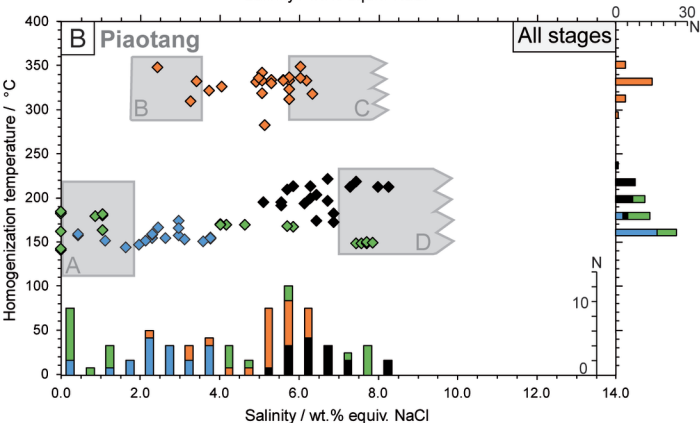
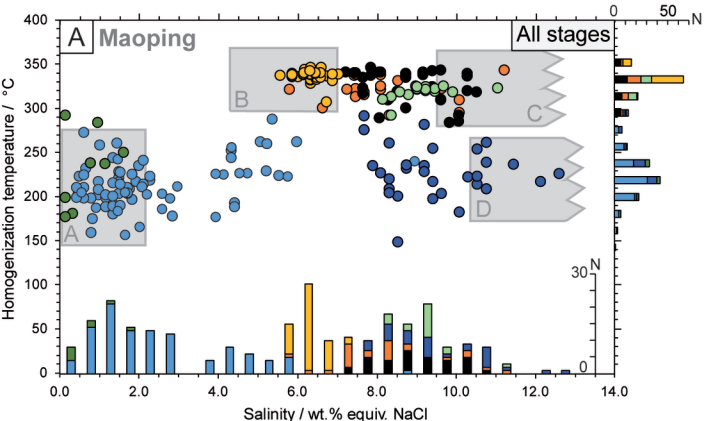












### Maoping

Stage III: W-Sn veins

● Quartz<sub>2-III</sub> (N=96)

● Wolframite<sub>1-III</sub> (N=30)

● Cassiterite<sub>1-III</sub> (N=25)

Stage IV: banded quartz veins

● Quartz<sub>4-IV</sub> (N=41)

Stage VI: late filling stages

● Fluorite<sub>1-VI</sub> (N=20)

● Topaze<sub>4-VI</sub> (N=46)

● Fluorite<sub>2-VI</sub> (N=15)

### Piaotang

Stage I: oxide-silicate stage

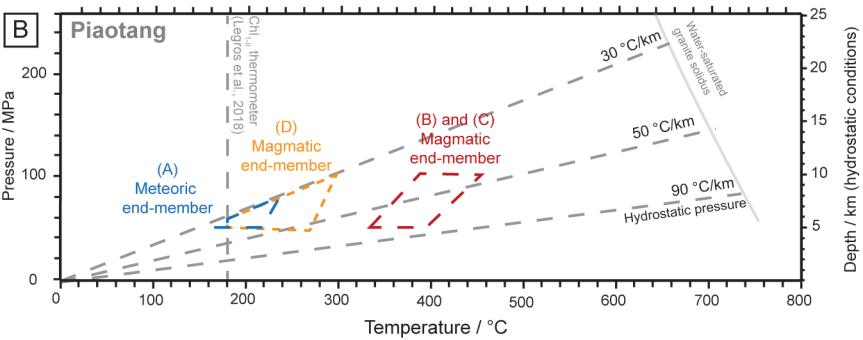
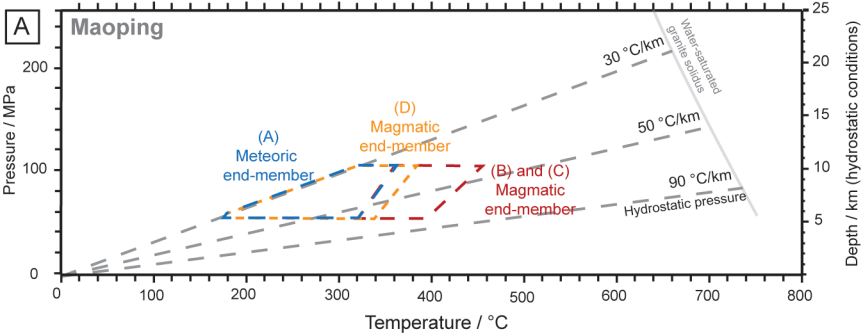
◆ Quartz<sub>1-I</sub> (N=20)

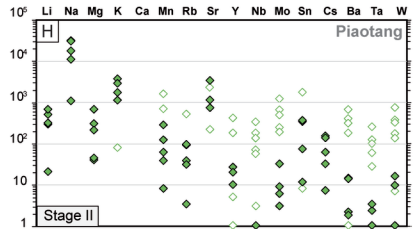
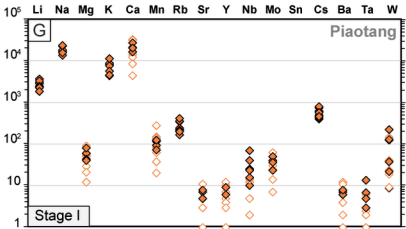
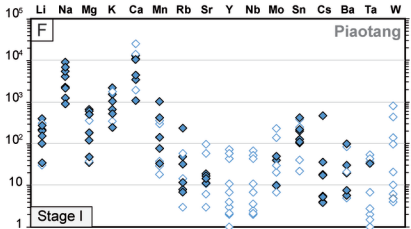
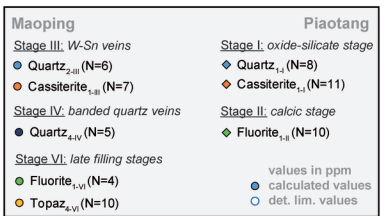
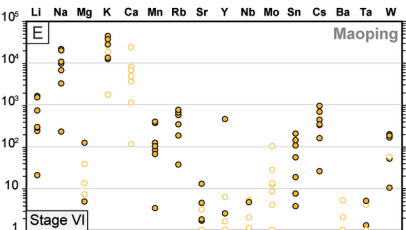
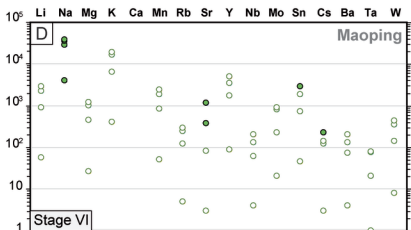
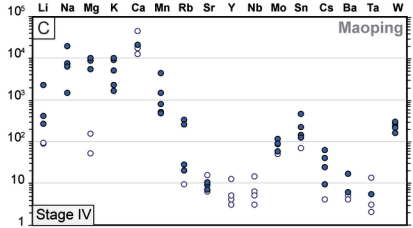
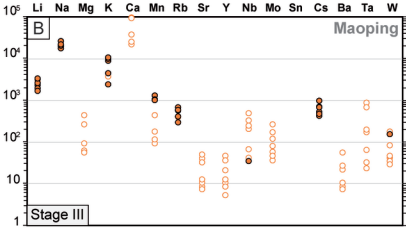
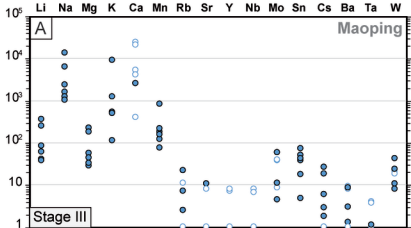
◆ Wolframite<sub>1-I</sub> (N=18)

◆ Cassiterite<sub>1-I</sub> (N=24)

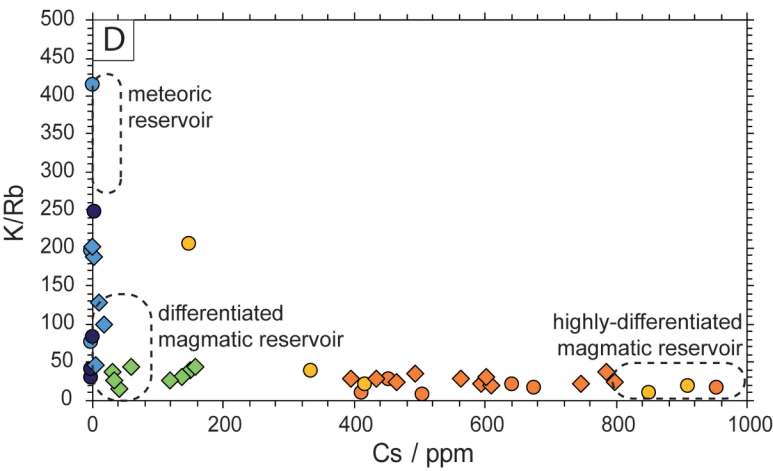
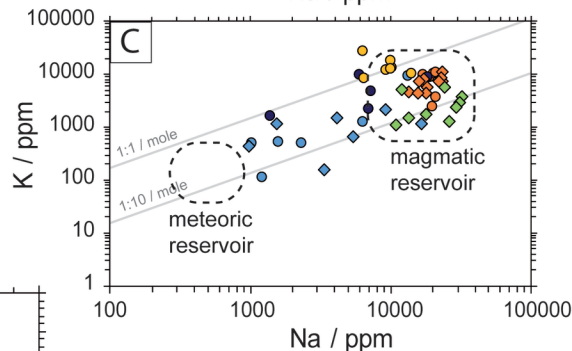
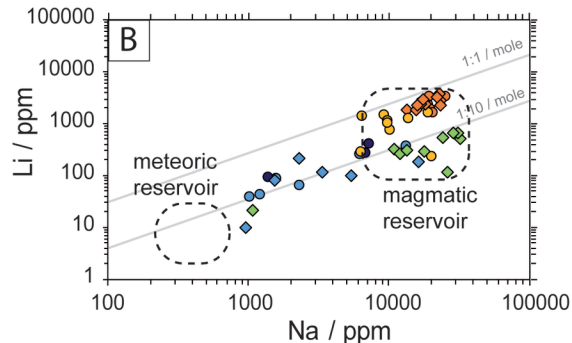
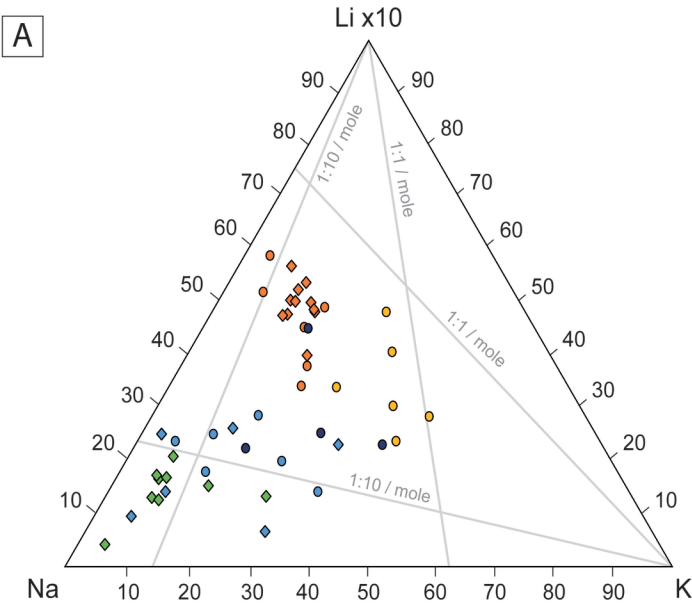
Stage II: calcic stage

◆ Fluorite<sub>1-II</sub> (N=23)









### Maoping

#### Stage III: W-Sn veins

● Quartz<sub>2-III</sub> (N=6)

● Cassiterite<sub>1-III</sub> (N=7)

#### Stage IV: banded quartz veins

● Quartz<sub>4-IV</sub> (N=5)

#### Stage VI: late filling stages

● Fluorite<sub>1-VI</sub> (N=4)

● Topaz<sub>4-VI</sub> (N=10)

### Piaotang

#### Stage I: oxide-silicate stage

◆ Quartz<sub>1-I</sub> (N=8)

◆ Cassiterite<sub>1-I</sub> (N=11)

#### Stage II: calcic stage

◆ Fluorite<sub>1-II</sub> (N=10)

